HHS Public Access

Author manuscript

Nature. Author manuscript; available in PMC 2019 July 02.

Published in final edited form as:

Nature. 2019 January ; 565(7739): 361–365. doi:10.1038/s41586-018-0823-6.

A Wireless Closed Loop System for Optogenetic Peripheral Neuromodulation

Aaron D. Mickle[#1,2], **Sang Min Won**[#3], **Kyung Nim Noh**[#3], **Jangyeol Yoon**[#4], **Kathleen W. Meacham**[1,2], **Yeguang Xue**[5,6], **Lisa A. McIlvried**[1,2], **Bryan A. Copits**[1,2], **Vijay K. Samineni**[1,2], **Kaitlyn E. Crawford**[7], **Do Hoon Kim**[4], **Paulome Srivastava**[1,2], **Bong Hoon Kim**[4,10,12,13], **Seunghwan Min**[4], **Young Shiuan**[1,2], **Yeojeong Yun**[4], **Maria A. Payne**[9], **Jianpeng Zhang**[8], **Hokyung Jang**[4], **Yuhang Li**[8], **H. Henry Lai**[1,2,9], **Yonggang Huang**[5,6,10], **Sung-Il Park**[11], **Robert W. Gereau IV**[1,2,*], and **John A. Rogers**[4,6,10,12,13,14,15,16,*]

[1]Washington University Pain Center and Department of Anesthesiology, Washington University, St. Louis, MO, 63110, USA

[2]Washington University School of Medicine, 660 S. Euclid Ave, Box 8054, St. Louis, MO, 63110, USA

[3]Department of Electrical and Computer Engineering, University of Illinois at Urbana-Champaign, Urbana, IL, 61801, USA

[4]Department of Materials Science and Engineering, University of Illinois at Urbana-Champaign, Urbana, IL, 61801, USA

[5]Department of Civil and Environmental Engineering, Northwestern University, Evanston, IL 60208, USA

[6]Mechanical Engineering, Materials Science and Engineering, Northwestern University, Evanston, IL 60208, USA

[7]Department of Materials Science and Engineering, University of Central Florida, Orlando, FL 32816, USA

[8]Institute of Solid Mechanics, Beihang University (BUAA), Beijing, 100191, China

[*]Corresponding authors. jrogers@northwestern.edu; gereaur@wustl.edu.

Author contributions:

ADM, SMW, KNN and JY contributed equally to the work; ADM, SMW, KNN, KWM, JY, SIP, JAR and RWG conceived of and designed experiments/material devices; SMW, KNN, JY, KEC, SM, DK, YY, SIP designed and provided optoelectronic devices; SMW, KNN, JY conducted all bench top tests; SMW provided device illustration; YX, JZ, YL, and YH contributed to mechanical and thermal simulations; ADM performed all surgical implantations and viral injections; ADM, LAM, PS, YS collected and analyzed histological data; ADM preformed and analyzed data from cytometry stain gauge, gait analysis; VKS collected and analyzed data from open field experiments; MAP collected and analyzed VMR data; LAM, BAC collected and analyzed data for the electrophysiology experiments; ADM, SMW, KNN designed and tested the closed loop algorithm. KNN programed and tested the iOS software; HHL provided guidance and resources for cystometric and metabolic studies; ADM, SMW, KNN, JAR and RWG wrote the manuscript.

Conflict of Interest:

JAR and RWG are co-founders of Neurolux, a company that manufactures wireless optoelectronic devices. The device described here uses similar technology, however is distinct from the current Neurolux portfolio.

Data and materials availability

The data that support the findings of this study are either provided in the source data or are available from the corresponding author upon reasonable request. iOS code is available at https://github.com/noh21/bladder_cloc

[9]Washington University Department of Surgery - Division of Urologic Surgery, St. Louis, MO, 63110, USA

[10]Materials Science and Engineering, Northwestern University, Evanston, IL 60208, USA

[11]Department of Electrical and Computer Engineering, Texas A&M University, College Station, TX. 77843, USA

[12]Simpson Querrey Institute, Northwestern University, Chicago, IL 60611, USA

[13]Center for Bio-integrated Electronics, Northwestern University, Evanston, IL 60208, USA

[14]Department of Biomedical Engineering, Northwestern University, Evanston, IL 60208, USA

[15]Department of Chemistry, Northwestern University, Evanston, IL 60208, USA

[16]Department of Neurological Surgery, Feinberg School of Medicine, Northwestern University, Chicago, IL 60611, USA

[#] These authors contributed equally to this work.

Summary Paragraph

The fast-growing field of bioelectronic medicine aims to develop engineered systems that relieve clinical conditions through stimulation of the peripheral nervous system (PNS)[1–5]. Technologies of this type rely largely on electrical stimulation to provide neuromodulation of organ function or pain. One example is sacral nerve stimulation to treat overactive bladder, urinary incontinence and interstitial cystitis/bladder pain syndrome[4,6,7]. Conventional, continuous stimulation protocols, however, cause discomfort and pain, particularly when treating symptoms that can be intermittent in nature (e.g. sudden urinary urgency)[8]. Direct physical coupling of electrodes to the nerve can lead to injury and inflammation[9–11]. Furthermore, typical therapeutic stimulators target large nerve bundles that innervate multiple structures, resulting in a lack of organ specificity. This paper introduces a miniaturized bio-optoelectronic implant that avoids these limitations, via the use of (1) an optical stimulation interface that exploits microscale inorganic light emitting diodes (μ-ILEDs) to activate opsins, (2) a soft, precision biophysical sensor system that allows continuous measurements of organ function, and (3) a control module and data analytics approach that allows coordinated, closed-loop operation of the system to eliminate pathological behaviors as they occur in real-time. In an example reported here, a soft strain gauge yields real-time information on bladder function. Data analytics algorithms identify pathological behavior, and automated, closed-loop optogenetic neuromodulation of bladder sensory afferents normalize bladder function in the context of acute cystitis. This all-optical scheme for neuromodulation offers chronic stability and the potential for cell-type-specific stimulation.

This fully implantable, wireless neuromodulation system combines a thin, low modulus strain gauge to monitor bladder filling/voiding with μ-ILEDs to control inhibitory opsins expressed virally in bladder sensory afferents. To achieve the desired closed-loop control of bladder dysfunction, the entire integrated platform includes five interconnected sub-systems; 1) a low-modulus, stretchable strain gauge that encircles the bladder to measure bladder activity (filling/voiding), 2) a pair of μ-ILEDs that deliver light directly to the bladder for optogenetic neuromodulation, 3) a thin, soft base-station that inserts between the abdominal

skin and muscle for bidirectional communication and wireless control of the μ-ILED actuators, 4) a wireless harvesting unit that distributes power to the entire system and 5) customized software deployed on a handheld device to enable real-time visualization, storage and analysis of operational data, and to provide an automated control interface for setting illumination protocols and parameters for open- or closed-loop interventions (Fig. 1a,b). Sub-systems (1) & (2) and (3) & (4) integrate into two separate modules, electrically connected within the body of the animal by insulated fine wires. This system provides the critical advantage over other real-time bladder function measurements in that it does not require direct nerve interfaces or incisions in the bladder required for most pressure monitoring systems. Implantation of sub-systems (1) & (2), referred to as the opto-electronic stimulation and sensing module, involves conformal circumferential interfacing of the strain gauge with the bladder, secured by an integrated buckle with a small dissolvable suture to the detrusor muscle (ED Fig. 1a,b). Sub-systems (3) & (4), referred to as the wireless control and power (WCP) module, is a thin, flexible component that inserts subcutaneously in the abdomen (Fig. 1c,d). One month after implantation, the opto-electronic stimulation and sensing module and WCP module both remain in their original positions (Fig. 1e), with no signs of degradation in functionality or performance.

The opto-electronic stimulation and sensing module combines a thin (15 μm) layer of silicone doped with carbon-black as a strain gauge, with a pair of μ-ILEDs for optogenetic stimulation (Fig. 2a and ED Fig. 2a). A low modulus silicone material serves as the substrate and overall encapsulation. The entire platform encircles the bladder, such that dimensional changes in the bladder that occur with filling and voiding stretch the strain gauge. Resulting changes in resistance correlate to bladder volume (ED Fig. 2b,c). The shape of the opto-electronic stimulation and sensing module and its low modulus construction allow for reliable chronic function and durability in detection of bladder expansion (ED Fig. 2d,e). While the strain-stress curves obtained by dynamic mechanical analysis indicate that the modulus of the responsive material in the SG is 270 kPa, the overall modulus of the SG device is much lower, 70 kPa (Fig. 2b), achieved by embedding the narrow SG (thickness 15 μm) above and below with undoped silicone film (thickness 40 μm, modulus 60 kPa) (ED Fig. 2f). Finite element analysis of experimental measurements of changes in bladder dimensions caused by filling with saline (ED Fig. 2g-i) suggest that the modulus of the bladder wall is range between 10 and 40 kPa from empty to full, consistent with previous reports[12]. These modulus values allow finite element analysis simulations of the bladder radius, assuming a spheroidal shape, during expansion with and without the strain gauge (Fig. 2c). Deformations of the bladder due to the strain gauge are less than 2% of overall expansion due to filling, consistent with negligible mechanical loading (Fig. 2d). *In vivo* measurements of cystometric pressures during filling and voiding show no effects of the device, consistent with FEA results (Fig. 2e).

The μ-ILEDs are mounted on a thin, flexible substrate of stainless steel (25 μm) and exploit transparent layers of polyisobutylene and polydimethylsiloxane as frontside encapsulation (ED Fig. 3a). Activation of the μ-ILEDs causes 44.3 ± 10.9 μW of light (540 nm) to pass through the full thickness (non-stretched) bladder wall (ED Fig. 3b, c). The small dimensions of the μ-ILEDs and the high thermal conductivity of the stainless-steel result in efficient dissipation of thermal load associated with operation, even with continuous

illumination. Measurements indicate that one hour of constant illumination leads to increases <1˚C in the temperature of the contacting tissue (ED Fig. 3d-h).

To communicate strain gauge sensor readings to a user interface, the WCP module incorporates a low-powered radio frequency (RF)-embedded microcontroller and wireless power management circuitry (Fig. 2f,g and ED Fig. 4a). Power delivery to the WCP module occurs wirelessly via resonant inductive coupling through a three-coil wireless power transfer (WPT) link. The transmitter side incorporates a 13.56 MHz radio frequency identification (RFID) driver, impedance matching circuitry, and a primary coil. A secondary resonating coil wrapped around the bottom of the cage to enhance the efficiency of power transfer, and a load coil in the WCP module constitute the receiver end (ED Fig. 4b). Matching the impedance of the receiver coils such that they resonate at 13.56 MHz yields a loosely coupled WPT system, designed to alleviate sensitivities to mismatches in antenna characteristics and allow the WPT coverage throughout the rat cage. The received voltage on the parallel-resonant load coil is rectified with a full-bridge rectifier and regulated using a charge pump converter to simultaneously power the wireless system and charge a pair of supercapacitors within the WCP module. These supercapacitors act as a short-term energy buffer (two 70 mF supercapacitors with 720 mJ at 3.2 V) during periods when the wirelessly received power is insufficient to operate the system, typically caused by rotations of the animal (most commonly, rearing for 1-5 seconds) that lead to an angular mismatch between the load antenna on the WCP module and the primary transmission antenna (ED Fig. 4c). The supercapacitors can power the system for over 3 minutes without external power (ED Fig. 4d); wireless charging occurs in ~30 s when the transmitting antenna outputs 4W.

The full closed-loop optogenetic control (CLOC) system accurately monitors bladder activity, where large decreases in resistance (decreases in bladder size) correlate with voiding events as measured by a metabolic cage (Fig. 3a). Importantly, implantation of the CLOC system does not significantly affect bladder cystometric properties 7 days after implantation compared to animals that received a sham implantation surgery (ED Fig. 5a,b). This confirms that the strain gauge does not constrict the bladder, and that there is no significant formation of fibrosis around the bladder, which could decrease bladder compliance. Additionally, no significant inflammatory response, alterations to gait, movement, or weight changes occurred 7 days after device implantation compared to animals receiving sham surgery (ED Fig. 5c-h). Altogether, these results indicate that the implanted CLOC system accurately measures bladder function, has minimal effect on bladder physiology, and does not cause detectable harm or distress to the animal.

An optogenetic strategy allows for modulation of bladder function, enabled by injection of a herpes-simplex viral (HSV) vector containing genetic payload to express the inhibitory opsin archaerhodopsin 3.0 (Arch)[13] directly into the bladder wall. This approach enables specific neuromodulation of sensory afferents innervating the bladder as differentiated from traditional electric stimulation of the sacral root, which additionally activates neurons innervating the colon and other pelvic structures. Because HSV vectors provide tropism for sensory neurons[14], this injection results in expression of Arch in sensory neurons innervating the bladder; Arch protein is detectable in peripheral terminals in the bladder wall, as well as cell bodies of the dorsal root ganglion (DRG) neurons 7 days after injection

(Fig. 3b). Injection of viral vectors alone does not significantly alter cystometric properties or cause alterations in mast cell degranulation, a marker for inflammatory response, 7 days after injection (ED Fig. 6). Isolated bladder-projecting DRG neurons transduced with Arch-eYFP demonstrate reduced neuronal excitability on exposure to 530 nm light (ED Fig. 7a-e). Additionally, Arch activation reduces neuronal excitability in DRGs cultured from human donors and transduced with Arch-eYFP (ED Fig. 7e-k). Together these results illustrate that HSV vectors transduce the inhibitory opsin Arch in bladder projecting sensory neurons without overt tissue damage, and that activation of Arch in rat or human DRG neurons decreases neuronal excitability.

Anesthetized cystometry, a measure of bladder physiologic properties, reveals the effect of Arch-mediated neuronal inhibition on bladder function. In rats that express Arch-eYFP in bladder-projecting neurons, illumination of the bladder significantly increases the intercontraction interval (ICI) compared to rats expressing only eYFP (ED Fig 8a,b), as demonstrated with implanted opto-electronic stimulation and sensing module and intravesicular catheters to measure bladder pressure. These groups, however, show no differences in peak, baseline, or threshold pressures (ED Fig. 8c). Similar degrees of ICI delay appear in data collected using the strain gauges and intravesicular pressure sensors, providing further evidence that the opto-electronic stimulation and sensing module accurately measures bladder function.

Implanting CLOC platforms in animals that express Arch-eYFP or eYFP allows for the assessment of Arch activation on normal voiding in awake freely moving animals. Bladder illumination does not alter void frequency, or the time to first void during the 3-hour illumination period in Arch-eYFP/LED-ON, eYFP/LED-ON and virus-injected/LED-OFF groups (ED Fig. 8d). Rats previously treated with cyclophosphamide (CYP, 75 mg/kg, i.p), to induce voiding dysfunction[22], show significant increases in the frequency of voids but no significant increase in bladder nociception (ED Fig. 8e,f). Thus, under the present experimental conditions it was not possible to determine whether the system could also reduce cystitis-induced increases in bladder pain. In CYP-injected rats, bladder illumination results in a significant decrease in the number voids in the Arch-eYFP/LED-ON group compared to eYFP/LED-ON and virus-injected/LED-OFF groups, during the 3 hours post-injection (Fig. 3c,d). Additionally, a significant increase in the time to the first void after CYP injection appears in the Arch-eYFP/LED-ON group compared to the eYFP/LED-ON and virus-injected/LED-OFF groups (Fig. 3d).

Fully automated utilization of the CLOC system requires algorithmic identification of strain gauge data signatures of abnormal bladder voiding. Real-time signal processing methods classify abnormal bladder activity based on identification of voiding events, indicated by relatively prolonged increases in strain gauge resistance (increases in bladder size) followed by rapid decreases (rapid decreases in bladder size). Further, void volume can be estimated by evaluating change in resistance during the voiding event. Preliminary ‘training’ data from the strain gauge collected concurrently with data from the metabolic cage facilitates the development of signal processing methods that accurately differentiate voiding events from noise due to motion artifacts or other parasitic signals. Voiding events are identified by filtering the raw strain gauge data (1 Hz sampling rate) with a 60-point moving average,

down-sampling the results to 0.25 Hz, and then computing the derivative of these processed data (ED Fig. 9a). These steps suppress high frequency noise associated with non-voiding events, such as internal organ movement and motion artifacts, but retain voiding data that occur on timescales of 10-30 s. Analysis of these data shows that voiding events correlate strongly with three consecutive values of the derivatives that are less than a pre-set threshold. The value of this pre-set threshold corresponds to the standard deviation of one hour of strain gauge data, collected on each animal/device, to account for device-to-device and animal-to-animal variability. A final step rejects identified voids as false, if they occur shortly following instances of large rapid increases in the strain gauge response, a movement artifact that would represent a non-feasible bladder expansion. Altogether, this algorithm identifies voids with >85% accuracy in naïve animals and >95% after induction of abnormal voiding with CYP (ED Fig. 9b).

Analysis of the training data set indicated that in the context of CYP-induced cystitis, frequency (all animals observed greater than a two-fold increase in voids after CYP) is a more consistent indicator of the disease state than change in void size (ED Fig. 9c). We therefore only considered a change in void frequency (to three voids within one hour) as the beginning of the disease condition. However, in different contexts assessing volume may be critical, so we include an additional feature within the software to evaluate void volume compared to a threshold. If a void is larger than the threshold, it will be considered a “healthy” void, and is not counted toward closed loop activation. We have validated this functionality with an *in vitro* model, where larger simulated voids did not activate the closed loop system regardless of the intervals, while frequent smaller voids can activate the μ-ILED (ED Fig. 9d).

Closed-loop operation involves the execution of a software application that enables real-time processing of the signal, logging responses of the strain gauge for subsequent analysis, activating/deactivating of the μ-ILEDs and implementing the analysis algorithms described above. The application also includes a user interface to define variables including derivative thresholds for identifying voiding events. When the patterns of voiding meet the criteria defined by these input values (three voids per hour, as informed by our training data), the μ-ILEDs activate for 2 hours (Fig. 4a).

Seven days after viral transduction of Arch-eYFP or eYFP and CLOC system implantation, the closed loop software was initiated. The closed-loop software does not activate the μ-ILEDs prior to CYP-injection. However, ~4 hours after CYP injection (150 mg/kg, i.p.) the closed loop software activates the μ-ILEDs (Fig. 4b). Activation of the μ-ILEDs results in a reduction in the frequency of voiding in the Arch-eYFP transduced animals compared to the eYFP controls, similar to the experimenter-initiated μ-ILED experiments (Fig. 3c,d). These results demonstrate the ability of the CLOC system to automatically recognize abnormal voiding patterns based on algorithmic detection of voiding events and conditional activation of μ-ILEDs to attenuate this CYP-induced increased voiding.

In summary, the fully wireless, implantable bio-optoelectronics systems reported here represent a unique class of technology that allows for closed-loop modulation of peripheral organ function by combined, coordinated operation of a soft, biophysical sensor for

feedback control and a proximal light source for optogenetic stimulation. The results illustrate that the approach of utilizing virally delivered opsins as PNS neuromodulators[15–21] can be effective in normalization of bladder dysfunction in freely moving animals. Further extension of this work could utilize excitatory opsins to stimulate bladder contractions in the context of underactive bladder. Our prior work in mice[22] and preliminary data in rats suggest that voiding can be enhanced using a similar optogenetic approach. However, further refinement of viral targeting strategies would be necessary to avoiding targeting nociceptive afferents and thus causing pain.

To explore potential translatability of this viral approach, we demonstrate that Arch activation can successfully decrease excitability of human DRG neurons in a manner similar to what we show in rats (ED Fig. 7). Initial clinical trials utilizing opsins are underway[23,24] but demonstration of the safety and efficacy of chronic opsin expression are needed to realize the full therapeutic potential of optogenetic neuromodulation. Furthermore, light delivery technology would need to be scaled to provide adequate illumination to the much thicker and larger volumes of tissue in the human bladder.

Although the current study demonstrates the utility of this approach in monitoring and modulating bladder function, the core ideas and the supporting technology platforms can be easily adapted to address a range of application possibilities beyond those associated with the bladder. For example, the opto-electronic stimulation and sensing module can be modified to integrate multiple biophysical (temperature, flow, pressure, etc) and/or biochemical (metabolites, proteins, hormones, etc) sensors, and can be configured with various types of actuators (optical, electrical, pharmacological, etc.) to provide the desired modulation, all using control provided by adapted forms of the WCP module and data analytics approaches at the software level. In this sense, the platforms introduced here have versatile uses in pre-clinical and clinical studies into physiology and pathophysiology of the PNS. Altogether, this system and set of supporting demonstration studies provide a framework for future closed-loop technologies suitable for treatment of diseases effecting the PNS, offering alternatives to non-specific pharmacological or electrical stimulation approaches.

Methods

Fabrication of the wireless control/power (WCP) module

The first step involved spin-casting a polyimide (PI) film on a copper foil. Laminating the sheet, with the PI side down, onto a glass slide coated with polydimethylsiloxane (PDMS) enabled patterning of the copper layer into a coil geometry by photolithography (photoresist AZ 4620; spin-casting at 3000 rpm for 30 s, baking on a hot plate at 110°C for 3 min, UV irradiance for 300 $mJ \cdot cm^{-2}$, and development for ~40 s with developer AZ 400K/deionized water solution of 1:3 volume ratio) and wet etching (CE-100 copper etchant, Transense; ~2 min with frequent rinsing by water). Dry etching (Reactive-ion etching; 20 sccm O2, 200 mTorr, 150 W, 1800 s) removed the PI everywhere except underneath the copper traces. A cellulose-based, water soluble tape (e.g., Aquasol Corporation, ASWT-2) allowed retrieval of the structure from the PDMS/glass substrate. Deposition of a bilayer of Ti/SiO2 on the backside of the structure allows covalent bonding to a base layer of PDMS following

exposure of the PDMS layer to ultraviolet induced ozone (UVO). Here, the PDMS surface and ultraviolet lamp in the UVO cleaner chamber (144AX, Jelight Company Inc.) was maintained at 1 cm during a treatment time of 7 minutes. After removing the water-soluble tape, solder joints formed between the electronic components and corresponding bond pads on the Cu/PI platform yielded functional systems. Layers of polyisobutylene (PIB) and PDMS served as encapsulation.

Fabrication of the optoelectronic stimulating component

Extended figure 3a presents a schematic cross-sectional illustration and layout of the microscale inorganic light emitting diodes (μ-ILED). Solder joints and epoxy electrically and mechanically bonded two μ-ILEDs (TR2227, Cree) onto a polyimide substrate with exposed traces of copper. A similar strategy bonded a pair of copper wires in a polyurethane tube (PU-025, SAI infusion technologies) onto copper metal pads at the opposite end of polyimide substrate to serve as the interconnection between the u-ILEDs and the WCP module. This component was mounted onto a stainless-steel casing with epoxy (Loctite epoxy marine) coated on the back side. Dip coating followed by a thermal curing process step formed an encapsulating layer of PIB (two coats) and PDMS (three coats) on the light illuminating anterior, or bladder facing side, of the opto-electronic stimulation and sensing module.

Fabrication of the strain gauge (SG) component

Extended figure 2a presents a schematic cross-sectional illustration and layout of the SG. A thin layer of silicone elastomer (Ecoflex-0030, 40 μm thickness) on a water soluble film of poly(vinyl alcohol) served as a support for a piece of screen printed silicone doped with carbon-black (XC-72R, Fuel Cell Store) at 15% by weight. This carbon-black strain gauge is conceptually similar to a prior reports[27,28]. Patterns of copper formed on the polyimide substrate, attached to the carbon black doped silicone ends, provided means for electrical measurement. Silver (H20E Epo-Tek, TED PELLA) paste and epoxy (Loctite epoxy marine) mechanically and electrical secured the junctions. A spin-cast overcoat of silicone provided encapsulation. A mechanical cutting process defined the final shape of the device. Mechanical bench tests confirmed the sg functionality and durability after repeated mechanical deformation (ED Fig. 10)

Experimental subjects

Adult (200–300 g) female Sprague Dawley rats (Taconic) housed in pairs with access to food/water ad libitum were maintained on a 12 h:12 h light:dark cycle (lights on at 6:00 AM). All procedures unless specifically stated were performed during the light cycle. All experimental procedures were approved by the Animal Care and Use Committee of Washington University and in strict accordance the United States *National Institute of Health (NIH) Guide for the Care and Use of Laboratory Animals.*

Surgical implantation of the optoelectronic device

The whole device was first sterilized using ethylene gas, then the opto-electronic stimulation and sensing module was implanted around the bladder with the μLEDs facing the bladder.

The strain gauge first was secured around the bladder with the lower band (ED Fig. 1b [1-3]). Kwik-Sil adhesive (World Precision Instruments) was used to secure the strap to the base of the device (near the μLEDs), then the top buckle was passed through the connective tissue on the back of the bladder and connected to the other side of the T-shaped buckle (ED Fig. 1b [4]). A small absorbable suture (Plain Gut 6-0, Covidien) was placed through the band and into the smooth muscle layer of the bladder being careful not to puncture into the bladder lumen (ED Fig. 1b [4-5]). The wires, connecting to the wireless control/power (WCP) module, were then externalized through the abdominal muscle layer, then muscle was closed with sutures (Silk 4-0, Covidien) (ED Fig. 1b [6]). The WCP (3 × 3 × 0.3cm) was implanted between the skin and muscle (subcutaneously) ventral and rostral to the muscle incision and the skin was closed with surgical staples (ED Fig. 1b [7-9]). Sham surgeries followed the same protocol and timing without implantation of the device. Both wirelessly powered and battery powered devices were implanted and used throughout the following experiments.

Computed tomography (CT) imaging

CT images were taken from rats 1 month after implantation of the closed-loop optogenetic control (CLOC) system with a Siemens Inveon Micro PET/CT Scanner.

Dynamic mechanical analysis

A dynamic mechanical analyzer (Q800 DMA; TA Instruments) served as a tool for determining Young's moduli through analysis of measured strain-stress curves. The measurement involved a film tension clamp, a strain rate of 1% / min, a maximum strain of 25%, all performed under ambient conditions. Here, we selected the upper limit strain rate of 1% knowing that the modulus measured at 1% would likely be the highest observed in an awake animal experimental setting.

Extraction of mechanical properties of the rat bladder wall

The mechanical properties of the bladder wall can be extracted from measurement of the expansion of bladder as a function of pressure of saline delivered to its interior. Models of this type of pressure-deformation data approximate the bladder as a shell of spheroidal shape, with initial equatorial radius a_0 and length of the other semi-axis b_0, and initial thickness t_0 (initial thickness of 0.81 mm). Previous studies show that the shape of bladder (ratio b_0/a_0) has little effect on the pressure-volume relationship[29,30]. As a result, the spheroidal shape can be approximated as a spherical shell with the same inner volume [the equivalent radius is $(R_0)_{eq} = \sqrt[3]{a_0^2 b_0}$]. After expansion, the equivalent radius is determined as $R_{eq} = \sqrt[3]{a^2 b}$, where a and b are lengths of semi-axes of the bladder wall after expansion.

Mechanical analysis gives the nominal biaxial stress in the bladder wall as[31]

$$\sigma = \frac{P\pi R_{eq}^2}{2\pi (R_0)_{eq} t_0} = \frac{P R_{eq}^2}{2 (R_0)_{eq} t_0}, \quad \text{(S1)}$$

where P is the difference between the inner and outer pressure of the bladder wall. The nominal biaxial strain is given by

$$\varepsilon = \frac{R_{eq}}{(R_0)_{eq}} - 1. \quad \text{(S2)}$$

When the bladder is fully empty ($2a_0$=3.52mm, $2b_0$=5.83mm), the difference between the inner and the atmospheric pressure is not zero but is instead 3.2 mmHg due to intra-abdominal pressure. In the modeling, the intro-abdominal pressure is subtracted from the actual applied pressure on the bladder wall (ED Fig. 2g, h).

The nominal biaxial stress-strain relationship obtained above is used to fit the Ogden hyperelastic model. Its corresponding uni-axial stress-strain relationship (Fig. 2b) is calculated with the fitted Ogden hyperelastic model. FEA shows the extracted stress-strain relationship from the spherical shell approximation to reproduce the expansion of bladder wall under inner pressure (ED Fig. 2i), which verifies the method described above.

Finite element analysis of bladder expansion

Full three-dimensional FEA was performed using the commercial software ABAQUS (ABAQUS 2016). 6722 shell elements (ABAQUS element type S4R) were used for modelling of the bladder and 28800 solid elements (ABAQUS element type C3D8R) for the strain gauge. The mechanical properties of the bladder wall are described by its nominal bi-axial stress-strain relation obtained from pressure-expansion data (ED Fig. 2g) as described in previous section, and then fitted with Ogden hyperelastic model.

Nonlinear Mooney-Rivlin hyperelastic model was used to characterize mechanical behavior of the strain gauge band (including carbon black doped silicone and undoped neat silicone encapsulation), and material constants in the model were determined by fitting with measured initial modulus (270kPa and 60kPa for doped and undoped silicone, respectively). In simulation, the initial length of the strain gauge is taken as 15 mm, which allow the conformal contact on an experimentally measured diameter of specific bladder at contraction state (ED Fig. 2g).

Light penetration through the bladder

To measure the light penetration, a rat bladder was removed, 7-18 days post CLOC implantation and placed over a light sensor (Thor Labs, Power meter - PM100D; Sensor - S121C). A syringe inserted in to the neck of the bladder and secured with a suture (4-0 Silk) allowed for manual inflation with saline. The μ-ILEDs were placed on top of the bladder, directly in contact with the bladder surface and powered to the same intensity for each experiment. Light power recordings were made with the bladder in the fully inflated and empty states, each with and without μ-ILED illumination to account for ambient light. The bladder was then cut open and a sheet of bladder tissue was placed on the sensor for measurements of light transmission.

Thermal finite element analysis of operation of a μ-ILED

The calculations of the temperature increase with time were obtained by finite element analysis using ABAQUS commercial software (ABAQUS 6.14). The μ-ILED device (4 × 1.1 × 0.7 mm) consists of PDMS (390 μm thick), PIB (10 μm thick), epoxy (195 μm thick), copper (8 μm thick), PI (12 μm thick) and stainless-steel layer (25 μm thick) from top to bottom. The rectangular μ-ILED consists of a layer of SiC and InGaAs with length, width and thickness of 270 × 220 × 40 μm and 270 × 220 × 10 μm, respectively. The parameters used in the modeling include conductivity, density, and specific heat[32–34]. The blood perfusion rate was 0.008 ml/ml/s[35]. The computed temperature increases resulted from heat uniformly distributed across the rectangular surface of the μILED, with thermal output power of 70 mW/mm^2. The modeling results of temperature increment matched experimental findings (ED Fig. 3d and f). In the modeling, a full three-dimensional implicit transient heat transfer model with 2.5 million linear hexahedral DC3D8 elements is established. The schematic illustration of the opto-electronic stimulation and sensing module embedded in the tissue is shown in extended figure 3g. A convergence study has been carried out to ensure the accuracy of the model by increasing the number of elements for steady state analysis (ED Fig. 3h).

Wireless communication

Experiments used both battery-free and battery-powered devices (wireless powered devices were used in automatic identification of voiding (ED Fig. 9a) and demonstration of prolonged battery-free recording (ED Fig. 9e), all other wireless experiments utilized the battery powered design to allow for multiple short-term experiments to run concurrently). For the latter, a 90 mAh coin cell battery and a low-dropout regulator replaced the load-coil, impedance matching circuit, and power management circuitry of the former. The remaining circuitry consisted of the radio-embedded microcontroller (nRF51, Nordic Semiconductor) for wireless communication and the bridge circuit to measure the resistance of the strain sensor. A microcontroller embedded with a radio frequency transceiver and an analog to digital converter sampled measurements and controlled the μ-ILEDs. The resistance of the strain sensor was measured using a bridge circuit and an instrumental amplifier, converted with an internal analog/digital converter (ADC) in the microcontroller, and transmitted to a user interfacing device every second for further signal processing. A thin layer of copper (12 μm) and a ferrite shield placed at the base of the WCP module and patterned in the geometry of its constituent components magnetically shield the system from the incoming RF to minimize parasitic heating and noise of electronic components. A sampling rate of 1 Hz was sufficient to capture the bladder activity (~1 hour for bladder to fill and ~30 seconds void). Further signal analysis on the iOS application classified overactive bladder activity to determine when to activate the μ-ILEDs (current-controlled at 6.2 mA using a general-purpose input/output on the microcontroller).

Anesthetized cystometry

Rats were first anesthetized with urethane (U2500, Sigma), (two intraperitoneal (ip) injections totaling 2mg/kg, 1 hr apart; 0.8 and 1.2 mg/kg; stock solution 150 mg/ml) and then a midline incision was used to expose the bladder dome. After a small incision was

made in the dome of the bladder, a flared PE50 catheter (BB31695-PE/3, Scientific Commodities, Inc) was inserted into the dome of the bladder and secured with a purse string suture[36]. After the catheter was placed, if an LED strain gauge was used it was placed around the bladder as described above. The LED was then connected to a current source (U8031A, Adgilent) and controlled manually. The strain gauge was connected to a digital multimeter device (USB-4065, National Instruments) and data were recorded in (LabVIEW, National Instruments) with a developed script to measure changes in resistance. Then the syringe pump was started and the bladder was filled at 0.1 ml/min with room-temperature saline to evoke a regular voiding pattern. Intravesicular pressure was measured using a pressure transducer amplified by a Transbridge 4M amplifier (WPI) and recorded using WINDAQ data acquisition software (DataQ Instruments) at a sampling rate of 5 Hz. After a regular pattern was established, for experiments using the LED strain gauge, five consecutive contractions (4 intercontraction intervals) were recorded for baseline and then the LED was illuminated for the subsequent 5 contractions. This was repeated for each animal (total of 2 x). The first contraction after the light was turned on was not counted for either the baseline or LED period. For comparison of chronic strain gauge implantation vs. sham surgery and sham injection vs. viral injection, 1 hour of cystometric voiding was acquired from each animal after a stable pattern developed. Data were analyzed using a Matlab (Mathworks) script to determine baseline pressure (BP), threshold pressure (TP), maximum pressure (MP) and intercontraction interval (ICI) (terminology conformed to[37]). Compliance was calculated as (Flow rate × ($Time_{BP}$-$Time_{TP}$)) / (TP-BP). Rats that did not develop a regular cystometric pattern were excluded from analysis.

Novel environment exploratory behavior

To test if rats implanted with the CLOC device have altered exploratory behavior, we tracked movement in a novel environment (42 × 42 × 30 cm, length × width × height) 7 days after CLOC device implantation. Rat movement was tracked using a VersaMax Animal Activity Monitoring System (AccuScan Instruments, Inc., Columbus, OH) and distance traveled during the 30-minute test period was calculated.

Gait analysis

Gait analysis was performed using the automated gate analysis hardware (Catwalk XT 10.5, Noldus). Gait analysis was completed with the standard rat calibration (camera gain, green light intensity, run duration, run maximum variation). All animals were acclimatized to the Catwalk system 2x for 15 min, 1 day prior to testing. Rats were tested 7 days post CLOC device implantation. 4 compliant runs were required for each rat and parameters averaged.

Mast cell degranulation

Seven days after viral injection into the bladder (or sham injection), rats were deeply anesthetized with an intraperitoneal injection of ketamine cocktail (ketamine (100 mg/ml), xylazine 20mg/ml) and acepromazine (10 mg/ml)) and then transcardially perfused with 1x phosphate-buffered saline (PBS; pH 7.2) followed by cold 4% paraformaldehyde (PFA). Bladders were equilibrated in 30% sucrose, frozen in OCT (Tissue Tek), and 20 μm cross sections were thaw mounted directly onto SuperFrost plus slides (Fisher Scientific) using a cryostat. Slides were blinded and stained with acidified toluidine blue solution to visualize

mast cells [working solution of .002 g/mL toluidine blue O (Sigma) in 1% sodium chloride, pH 2.0-2.5]. Total numbers of mast cells were counted and added across three cross sections-one from each third of the bladder (base, middle, and dome). This was performed in duplicate and averaged. Cells were considered degranulated if there was an extensive dispersion of more than 15 extruded vesicles localized near the cell.

Viral transduction of bladder afferents

HSV-hCMV-eYFP and HSV-hCMV-Arch3.0-eFYP viral preparations were obtained from Massachusetts Institute of Technology viral core (Rachael Neve, MIT McGovern Viral Core Facility). The original Archaerhodopsin 3.0 (Arch) construct was cloned by the Deisseroth Lab. Viruses were obtained at a titer of ~3.5×10^9 infectious units per ml and diluted to 2.1×10^9 immediately before injection. Viral injections into bladder were performed to drive transgenic expression of eYFP or Arch selectively in peripheral bladder innervating neurons. After achieving and confirming full anesthesia using 3% isoflurane, a laparotomy was performed with a small transverse incision in the muscle and skin to expose the bladder. The bladder, if full was manually expressed to remove the majority of the urine. Then using a 35 ga Nanofil needle (WPI) and syringe 4 injections of 5 uL of either HSV-CMV-eYFP or HSV-CMV-Arch-eYFP (~2.1×10^9 infectious units total per injection) were made in to the bladder wall, equal distance apart around the base of the bladder. The needle was left in position for 1 min following each injection and then slowly removed to prevent leakage of the virus. Additionally, after all injections were completed, we waited an additional 5 mins before closing to allow for further undisturbed absorption. Next the muscle was closed with 5−0 nylon sutures and the skin was closed with surgical staples. Optogenetic experiments were then performed 6-8 days after injection.

Immunohistochemistry (Bladder Whole Mount)

Bladders were removed after transcardial perfusion with 1 × PBS, then cut from the base to the dome and pinned flat in a Sylgard dish. Bladders were covered with 4% PFA and fixed 4 hours to overnight. The urothelial/interstitial layers were then carefully dissected away from the smooth muscle layer. The bladder was washed again in 1× PBS 3 × 5 min and incubated in blocking solution (5% normal goat serum/0.3% Triton-X/1x PBS) for 2 hours at room temperature. The primary antibodies (1:1000 chicken anti-GFP, Aves GFP-1020) and 1:1000 rabbit anti-βtubulin, BioLegend 802001) were diluted in blocking buffer and incubated on the sections for 5-6 days at 4ºC with gentle agitation. Bladders were washed 5x for 15 min each with 1x PBS and then incubated with secondary antibodies in blocking solution for 2 hrs at room temperature (1:1000 goat anti-rabbit IgG Alexa Fluor 555, Thermo Fischer A21422, 1:1000 goat anti-chicken IgG Alexa Fluor 488, Thermo Fischer A11039). Samples then were washed 5x for 15 min with 1x PBS, and floated on to slides (Fisher Scientific), and coverslipped using Vector Shield hard set mounting media (Vectashield Hard Set). Whole mount samples were then imaged on a scanning confocal microscope (Leica). All whole mounts shown are from the urothelial/interstitial layers.

Immunohistochemistry dorsal root ganglion (DRG) and bladder H&E

DRGs were sectioned and stained as previously described[38]. Briefly, 6-8 days after HSV viral vector injection, rats were perfused with PBS and 4% PFA as described above. L6-S1

DRG were extracted, post-fixed in 4% PFA overnight, and then transferred to 30% sucrose for 24 hours. DRGs were then frozen in Tissue Tek Optimal Cutting Temperature (OCT) medium (Sakura Finetek), sectioned on a cryostat (Leica) at a thickness of 15 μM, and placed directly on slides. Slides were post-fixed with 4% PFA for 5 min, then thoroughly washed 3× 5-10 min. Slides were incubated with blocking buffer (1x PBS, 5% Goat serum, 0.3% triton-x) for 1 hour, followed by primary antibodies (1:1000 Chicken anti-GFP, Aves GFP-1020) and 1:1000 rabbit anti-βtubulin, BioLegend 802001) overnight at 4˚C. Slides were subsequently washed 3x with PBS and then incubated with the appropriate secondary antibodies (1:1000 Goat anti-rabbit IgG Alexa Fluor 555, Thermo Fischer A21422, 1:1000 Goat anti-chicken IgG Alexa Fluor 488, Thermo Fischer A11039) for 45 min at room temperature. Slides were finally washed 4× 10 min in PBS and coverslipped with Prolong Gold mounting media (P36934, Life Technologies). Slides were imaged on a confocal microscope and images processed using NIH Image J software. For H&E staining, the bladder was removed and then only the segment of bladder that contacted the band (or where the band would be in sham animals) was sectioned onto slides, which were post-fixed in ethanol and then stained with a standard H&E protocol[39]. For quantification of bladder thickness, 2x images of bladder were taken and the distance between lumen and the outer smooth muscle layer were measured in three locations and averaged by a blinded experimenter.

Rat DRG culture

Rats were injected with DiI (ThermoFisher, 10ul) into the bladder wall 7-10 days prior to DRG culture. DRG cultures were performed as previously described in mice[38]. Briefly, rats were anesthetized with ketamine cocktail and then quickly perfused with PBS. DRGs were removed and dissociated enzymatically with papain (Worthington) and collagenase type 2 (Sigma), and mechanically with trituration. Final solutions were filtered (40 μM, Fisher) and cultured with DRG media [5% fetal bovine serum (Gibco) and 1% penicillin/streptomycin (Corning) in Neurobasal A medium 1x (Gibco) plus Glutamax (Life Technologies) and B27 (Gibco)].

Human DRG culture

Human dorsal root ganglia (hDRG) extraction, dissection, and culturing was performed as described previously[40]. Briefly, in collaboration with Mid-America Transplant Services, L1-L5 DRG were extracted from a tissue/organ donor less than 2 hrs after aortic cross clamp. The donor was a 25 yo black female with a BMI of 21 and cause of death due to head trauma from a motor vehicle accident. hDRG were placed in an *N*-methyl-D-glucamine (NMDG) solution for transport to lab, fine dissection, and mincing. Pieces were dissociated enzymatically with papain (Worthington) and collagenase type 2 (Sigma), and mechanically with trituration. Final solutions were filtered (100μM, Fisher) and cultured with DRG media [5% fetal bovine serum (Gibco) and 1% penicillin/streptomycin (Corning) in Neurobasal A medium 1x (Gibco) plus Glutamax (Life Technologies) and B27 (Gibco)].

Viral transduction of DRG cultures

Rat and human DRG neurons were transduced with herpes simplex virus (HSV) carrying a transgene for the inhibitory proton pump Arch (HSV-hCMV-Arch3.0-eFYP). Virus was

added at a final concentration of 1.75×10^8 infectious units/ml either immediately after culturing (rat) or after 8-9 DIV (human). Neurons were used for electrophysiological recording from 24-48 hours post-transduction.

Whole-cell patch-clamp electrophysiology

Electrophysiological recordings from cultured rat and human DRG neurons were carried out in an external solution consisting of (in mM): 145 NaCl, 3 KCl, 2 $CaCl_2$, 1.2 $MgCl_2$, 7 Glucose and 10 HEPES, pH 7.3 with NaOH and ~305 mOsm. Patch pipettes were pulled from borosilicate glass electrodes, and had resistance values of 2-3 MΩ (human) and 3-4 MΩ (rat) when filled with (in mM): 120 potassium gluconate, 5 NaCl, 2 $MgCl_2$, 0.1 $CaCl_2$, 10 HEPES, 1.1 EGTA, 4 Na_2ATP, 0.4 Na_2GTP, 15 sodium phosphocreatine, pH=7.3 with KOH, 291 mOsm. Fluorescence imaging and photostimulation was performed using custom built LEDs (M470L2 and M530L3, Thorlabs) coupled to the epi-fluorescence port of an upright microscope (BX-51, Olympus). LEDs were positioned for Köhler illumination, and light intensity was calibrated using a photodiode (S120C, Thorlabs) and power meter (PM100D, Thorlabs). Recordings were made using Patchmaster software controlling a HEKA EPC10 amplifier, low-pass filtered (Bessel 10 kHz), and digitized at 20 kHz. Action potential thresholds were determined from a holding potential of −60 mV with a series of 1s depolarizing current injections in increments of 10 pA (rat) or 100 pA (human). Action potential frequencies were elicited in response to suprathreshold stimuli at 1-4 times rheobase, both before and during constant illumination with 530 nm green LED light at 3.3 or $10mW/mm^2$ (M530L3, Thorlabs). Series resistance was kept below 10 MΩ in all recordings. Data were analyzed offline using custom-written macros and the Neuromatic plug-in (http://www.neuromatic.thinkrandom.com) in Igor Pro (WaveMetrics; Portland, OR).

Bladder inflammation model

Cyclophosphamide (C0768, Sigma) is metabolized in to acrolein, which is excreted by the kidneys in the bladder where it causes bladder specific inflammation and increases voiding frequency[41]. A single dose of 75 mg/kg cyclophosphamide (CYP, i.p.) was used for the open – loop/user-controlled experiments (Figure 3 E and F). One injection of 150 mg/kg CYP i.p. was used for the closed loop experiments. CYP was used because it can cause increased voiding frequency with a single i.p. injection, other methods are more invasive (intravesical infusion) or take a long time to develop (stress induced increases in voiding)[42].

Assessment of Visceral Motor Reflex

The visceral motor reflex (VMR) was measured by recording abdominal electromyograph (EMG) in response to bladder distension as previously described[38,43]. Briefly, rats previously injected with either saline (vehicle) or 150 mg/kg CYP 16-24 hours before VMR recordings, were anesthetized with isoflurane (2%). They were then catheterized with a 24-gauge angiocatheter and abdominal electrodes were placed into the external oblique, to measure EMG responses. Then the anesthetic concentration was slowly tapered down to 1.25%. After stabilization at the lower anesthetic concentration, phasic urinary bladder distensions (20-70mmHg) were delivered through the angiocatheter and corresponding EMG responses recorded. For analyses, baseline EMG was subtracted from the distension

response and the remaining EMG response was rectified and intergraded to collect the distension evoked EMG. All distensions were completed in triplicate and averaged for each individual animal.

Open-loop/user controlled μLED experiments

Rats were injected with either HSV-CMV-eYFP or HSV-CMV-Arch-eYFP at day 0 and implanted with the CLOC system on day 3. On day 5 rats were acclimated in modified metabolic rat cages above computerized balances (Columbus Instruments) for at least 2× 45-60 min sessions at least 1 hour apart. On day 6 they were put in the metabolic cage or kept in home cage in the same room and the μ-ILEDs were turned on or left off for 3 hours, depending on the treatment group. Some experiments were performed in metabolic cages to confirm voiding events to understand the relationship between SG resistance and voids (training set). On day 7 rats were injected with CYP (75 mg/kg, i.p.) at the same time of day as the baseline test and put in the metabolic cage or left in the home cage. μ-ILEDs were turned on (or not) and strain/metabolic data was recorded for 3 hours. All void analysis was done posthoc (Microsoft Excel). If an animal did not void within the 3 hours a value of 180 minutes was assigned. Voids were identified by methods outlined below.

Void identification signal analysis and verification

To identify voiding events, raw strain gauge data were analyzed using multiplestep signal processing. Standard deviation (SD) was calculated from each animal to account for device-to-device variability in noise and degree of change during filling and emptying events. The SD was taken from ~1 hour of raw data without a void. Raw data voids were identified by the following 4 steps: 1) take a moving 60-point (1 min) average 2) down sample to 4 points per second (from 1 pt per second) 3) calculate the derivative of the down sampled data 4) if three consecutive derivative values are less than 3X the negative SD, this is counted as a preliminary void. There are two conditions when preliminary voids calculated in this way are rejected: when there was a void in the previous 5 min and if there was a significant positive derivative value, indicating animal movement, preceding the void. A significant positive derivative value was calculated by averaging only the positive derivative values from the previous 10 points (2.5 min). If this value was higher than 40% of the SD (with a minimum value of 7) then the preliminary void was eliminated and counted as noise.

User interface (UI) and voiding identification

Software developed using XCode and operating on a tablet computer (iPad mini 2 and iPad Air 2, Apple) served to capture and compile SG data. The iOS application 1) logs SG data for post-data analysis, 2) defines μ-ILED protocols for optogenetic activation, and 3) sets calibration parameters for closed-loop experiments. Also, the UI displays 30 min graphical plots of raw, filtered, and derivative SG data for troubleshooting. iOS code is available at (https://github.com/noh21/bladder_cloc).

Operationally, the application first logs SG data (sampled at 1Hz) in a text file format in the iOS device after establishing Bluetooth connection to the implanted WCP device. Comparing SG data with metabolic cage data sets the foundation the signal processing required for closed-loop function. Second, the manual μ-ILED switch and textboxes located

at the top of the GUI enables open-loop optogenetic experiments. Turning on the “Manual LED” switch activates an μ-ILED protocol that follows an on/off timing pattern defined in the text boxes. Lastly, the closed-loop experimental function engages after a series of open-loop experiments. The “Automated Closed-Loop” switch turns on closed-loop functionality with calibration parameters defined in the textboxes. The parameters “Device STD, Noise Threshold, and Voiding Interval” are calibration metrics determined via data collected before the closed-loop experiments to account for variances among devices and rats. A series of signal processing steps determine whether a voiding has occurred (described above). If three voiding events occur within a preset interval, the μ-ILED protocol is activated.

Closed loop experiments

Rats were injected with HSV-eYFP or HSV-Arch-eYFP and implanted with the CLOC system 6 days prior to the experiment. On day 6 post-operation day (POD) SG data was collected to calculate the SD to calculate the threshold for voiding, for each individual animal. On the morning of POD 7 (~0800) the closed loop program (Fig. 4c) was activated while the rat was in its home cage. At ~1200 the closed loop program was turned off and the animals were injected with 150 mg/kg CYP. The program was turned off to prevent accidental activation due to experimenter handling the animal. 15 minutes after the injection of CYP, the closed loop program was turned on. Data were analyzed as described above.

Statistics and Reproducibility

All experiments were performed in female rats (200 −300g) and were randomly assigned to control or experimental groups for virus injection, device implantation or culture. Sample sizes were determined from preliminary experiments using the software G*power for the appropriate type of statistical comparison. In the open and closed loop experiments, data was excluded from animals where the closed-loop bladder device malfunctioned or was damaged. All data was collected in a non-biased manner and experimenter was blinded to treatment for final analysis. Unpaired t-tests and Mann-Whitney tests, as well as one-way and two-way ANOVAs were performed as appropriate. P values <0.05 were considered statistically significant. All results are represented as mean ± SEM. Figure 2e was repeated 3 times, figure 3a was repeated more than 10 times, figure 3b was repeated 4 times, and figure 4b was repeated 3 times, all in biologically independent animals with similar results. See Supplemental Table 1 for all statistical details results.

Extended Data

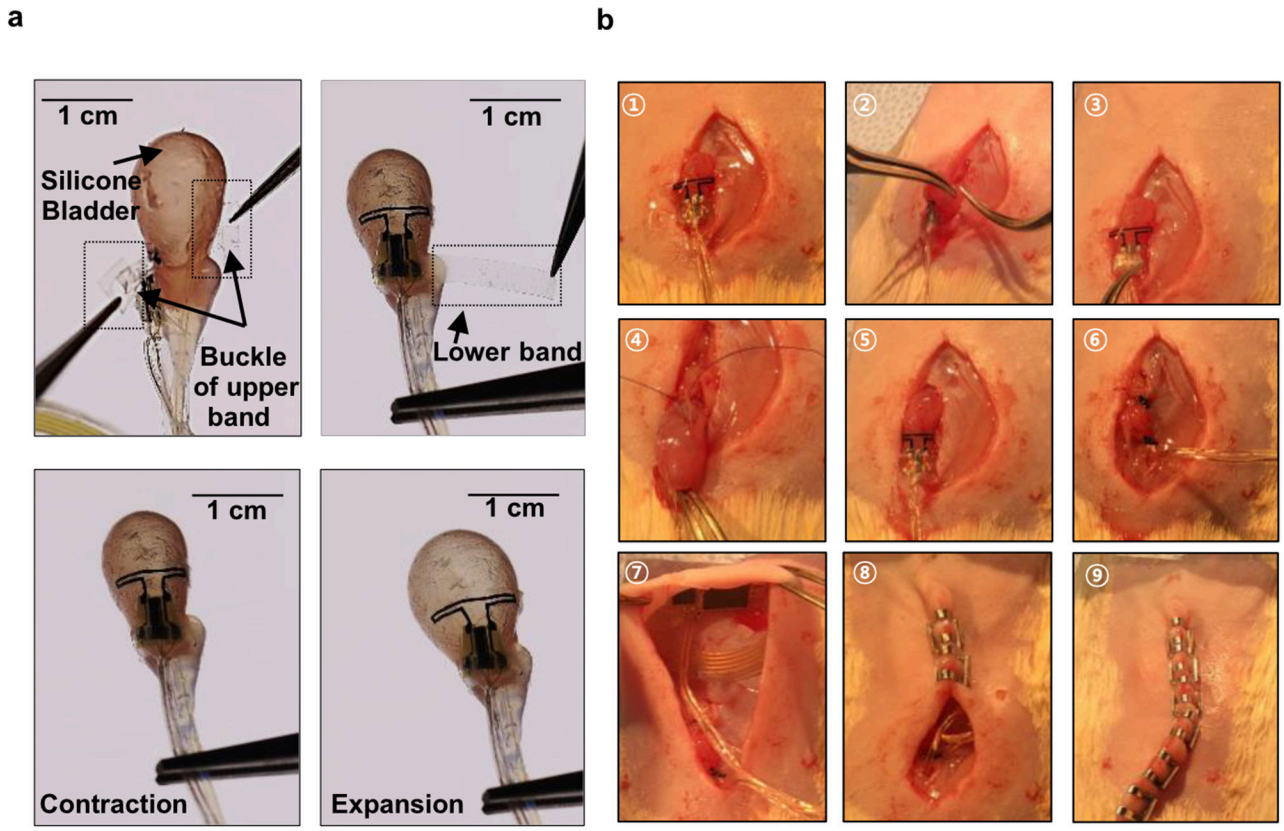

Extended Data Figure 1. Demonstration of opto-electronic stimulation and sensing module features and implantation of the whole CLOC system.

a) Demonstration of strain gauge placement on a mimic bladder illustrating the how the two silicone bands wrap around the bladder and how stretch is exerted on the strain gauge as the bladder expands. **b)** Detailed surgical procedure for implantation of the wireless closed-loop optogenetics-based system for peripheral neuromodulation. The strain gauge is placed on the bladder (1), using curved forceps, the lower band is pulled under the bladder and wrapped back on top of the opto-electronic stimulation and sensing module (2). Kwik-Sil is then applied to secure the lower band to the top of opto-electronic stimulation and sensing module (3). The upper band is then wrapped around the largest part of the bladder dome and the buckle secured. Then a small suture is placed through the buckle into the bladder smooth muscle layer to secure the upper band to the bladder (4). The bladder is then placed back in the abdominal cavity (5) and muscle layers closed with suture (6). The WCP is inserted between the skin and the muscle layer (6) and the skin is closed with surgical staples (8 and 9).

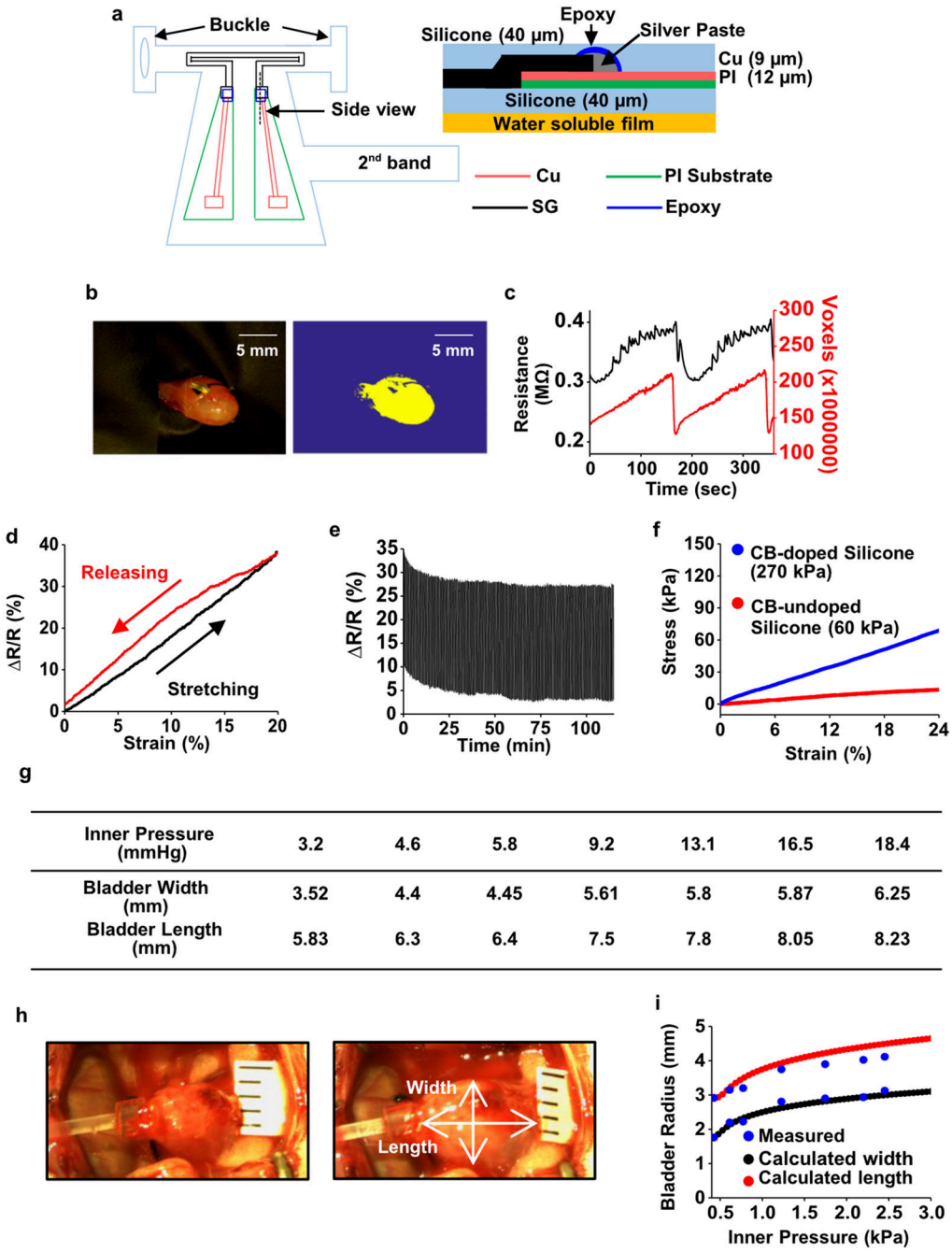

Inner Pressure (mmHg)	3.2	4.6	5.8	9.2	13.1	16.5	18.4
Bladder Width (mm)	3.52	4.4	4.45	5.61	5.8	5.87	6.25
Bladder Length (mm)	5.83	6.3	6.4	7.5	7.8	8.05	8.23

Extended Data Figure 2. Computational/experimental studies of the bladder strain gauge and material properties of rat bladder.

a) Schematic illustration of a strain gauge (SG), portion of the opto-electronic stimulation and sensing module. The right panel represents a cross-sectional side view of the device components at the level of the dashed line shown in the left panel. **b)** Image of a rat bladder (left) and digitally manipulated version (right) to allow measurements of the volumetric changes in size during cystometry. **c)** Graph of changes in bladder size (red) and changes in strain gauge resistance (black). **d)** Fractional change in resistance of the strain gauge as

function uniaxial tensile strain. **e)** Fractional change in resistance under 1000 cycles of stretching to a maximum strain of 20 %. **f)** Uniaxial strain-stress curve of carbon black-silicone composite and the undoped neat silicone. **g)** Length and width of the bladder measured using Vernier caliper, at different inner pressures. **h)** Representative optical image of a rat bladder at different inner pressure: 3.2 mmHg (left) and 18.4 mmHg (right) (Ruler marks 1 mm). **i)** Simulation results for the width and length of the bladder based on measured values of the inner pressure and the initial length and width.

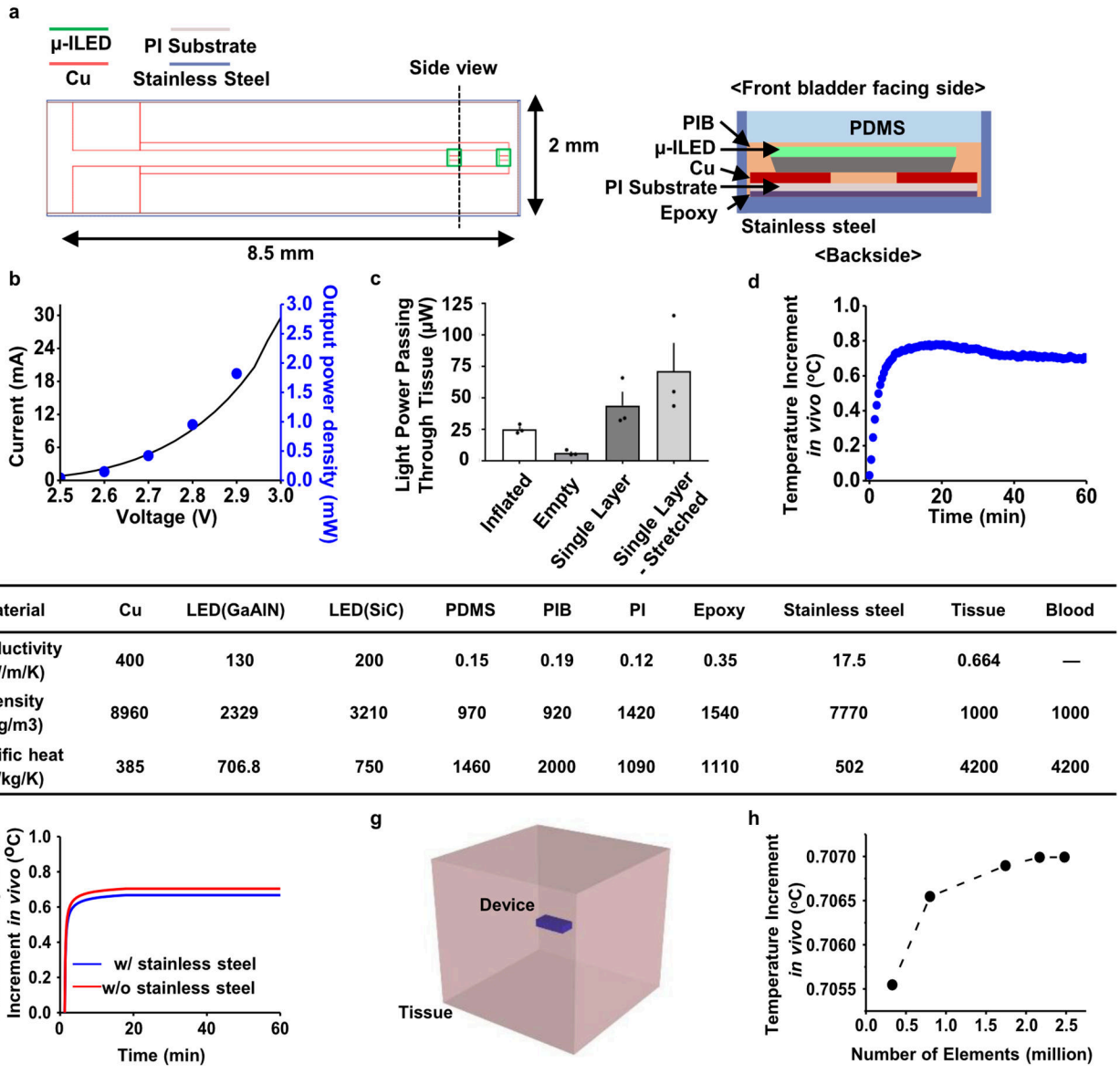

e

Material	Cu	LED(GaAlN)	LED(SiC)	PDMS	PIB	PI	Epoxy	Stainless steel	Tissue	Blood
Conductivity (W/m/K)	400	130	200	0.15	0.19	0.12	0.35	17.5	0.664	—
Density (kg/m3)	8960	2329	3210	970	920	1420	1540	7770	1000	1000
Specific heat (J/kg/K)	385	706.8	750	1460	2000	1090	1110	502	4200	4200

Extended Data Figure 3. Optical and Thermal characteristics of the μ-ILEDs.

a) Schematic illustration of the μ-ILED portion of the opto-electronic stimulation and sensing module. **b)** Electrical and optical characteristics of pair of μ-ILEDs. **c)** Measured power associated with penetration of light from a μ-ILED through the whole rat bladder

(both layers) at fully inflated and empty states, additional calculations were performed on single bladder layer relaxed and manually stretched. (performed in 3 biologically independent samples, mean ± SEM) **d)** Results from in vivo testing of the temperature associated with operation of the μ-ILEDs for an hour. **e)** The material properties in the model. **f)** Simulated results for the temperature associated with operation of the μ-ILEDs with and without the stainless-steel substrate. **g)** The schematic illustration of OESS module embedded in the tissue with dimensions of 30×30×30 mm^3 in FEA model. **h)** The effect of number of elements in FEA model on the temperature increment in vivo with power of 70 mW for steady state analysis.

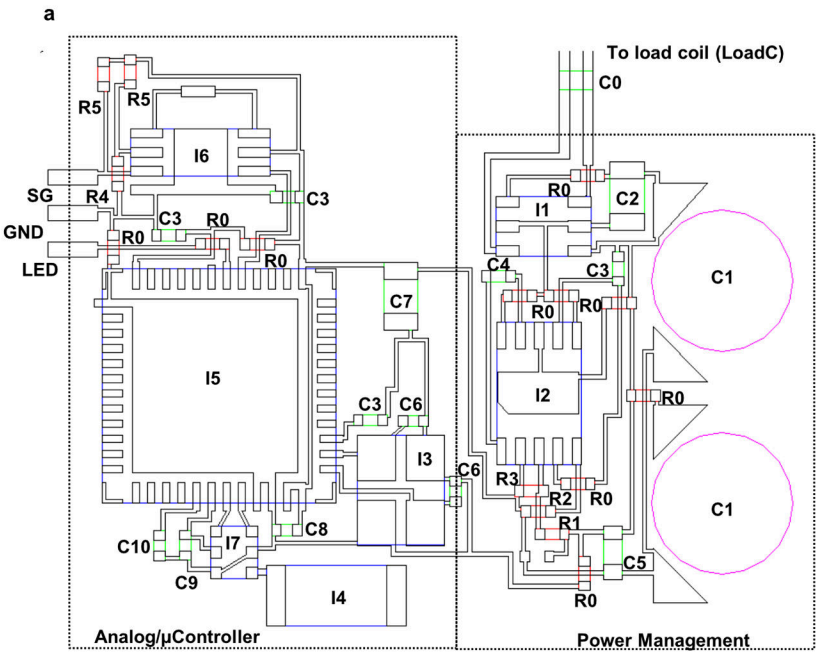

	Component	Product number
C0	86.5 pF	WCAP-CSGP 0402
C1	80 mF	XH414HG-IV01E
C2	1 μF	GRM033R71E102KA01J
C3	0.1 μF	CL03A104K03NNNC
C4	1 μF	CL03A105MP3ZSNH
C5	10 μF	CL05A106MP5NUNC
C6	12 pF	GRM0335C1E120GA01D
C7	47 μF	GRM188R60J476ME150
C8	10 pF	GRM033R71E102KA01J
C9	2.2 nF	GRM033R71A222KA01D
C10	47 nF	GRM033C80J473KE19D
R0	0 Ω	RC0603J000CS
R1	40.2 kΩ	RC0201FR-0740K2L
R2	220 kΩ	ERJ-1GEF2203C
R3	68 kΩ	ERJ-1GEF6802C
R4	22 kΩ	RC0201FR-0722KL
R5	1 MΩ	RC0201FR-071ML
I1	Schottky Diode	BAS40XY, 115
I2	DC Converter	LTC3255
I3	Crystal	CX2520DB16000D0WZRC1
I4	Antenna	2450AT18A100E
I5	Microcontroller	NRF51822
I6	Amplifier	INA333AIDGKR
I7	Balun	2450BM14E0003T

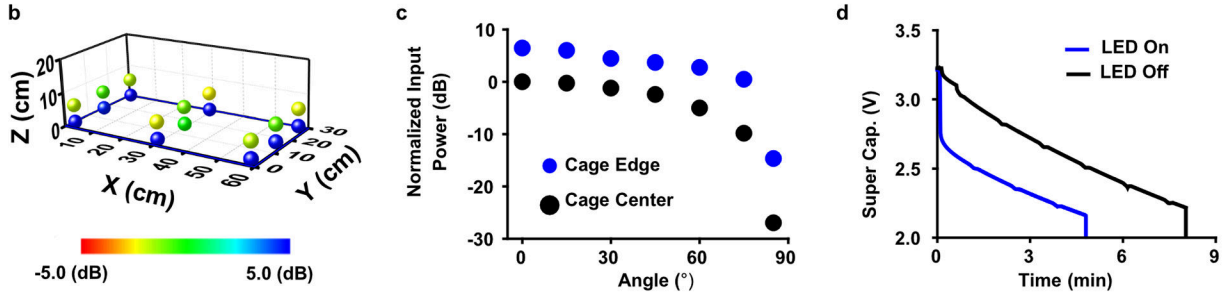

Extended Data Figure 4. Layout and operation of the wireless control and power (WCP) module. **a)** Layout and component information for the WCP module. **b)** Normalized wireless power distribution, in dB, inside the rat cage (30 cm × 60 cm) at heights of 0 and 5 cm from the ground. **c)** Normalized wireless power received, in dB, at different out-of-plane orientation angles of the receiver antenna relative to the transmission antenna, for positions at corner and center of the cage. **d)** A plot of the supercapacitor voltage, which is proportional to the

stored energy, as a function of time after deactivating the transmission antenna while the system is otherwise fully operational.

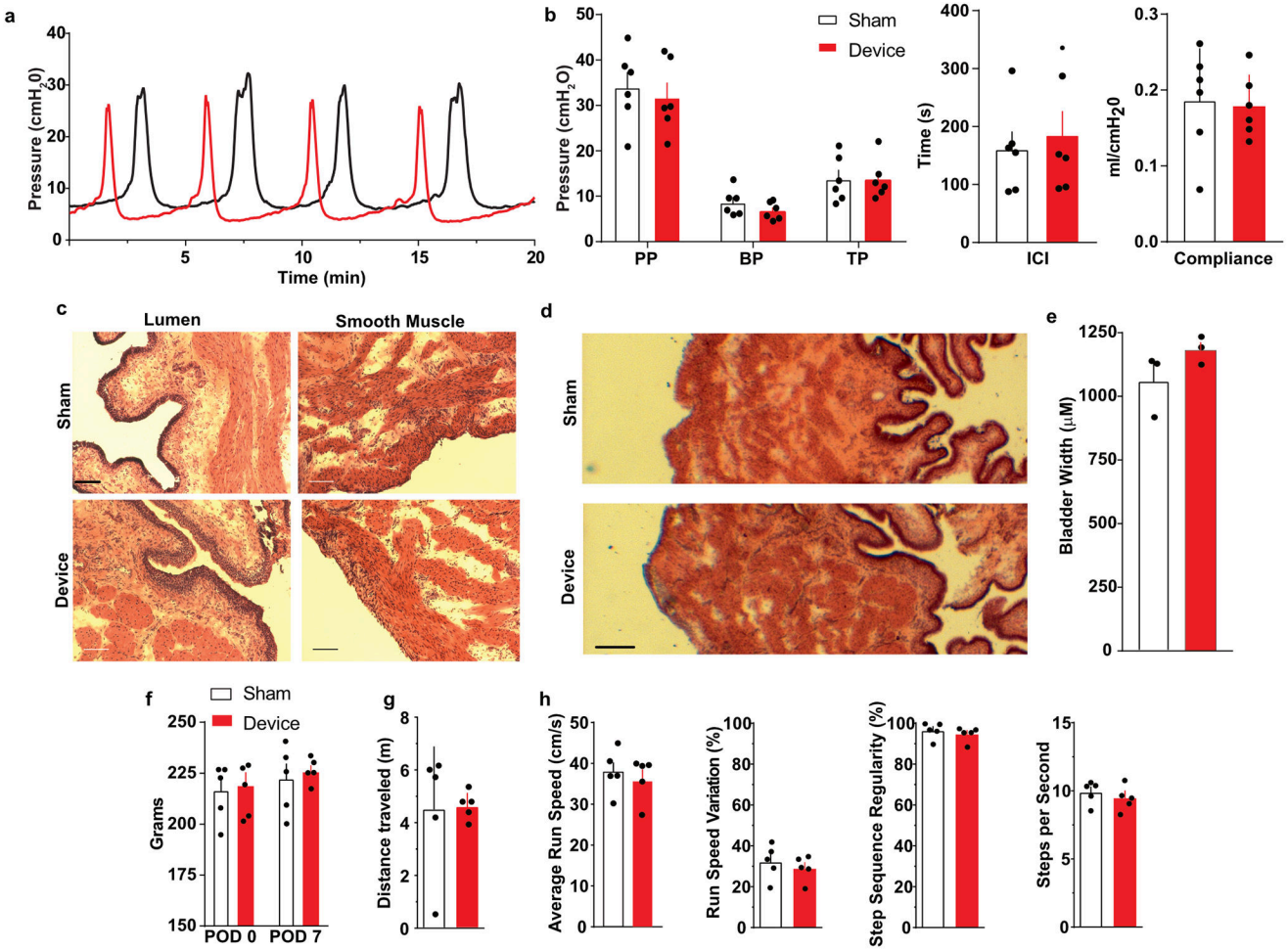

Extended Data Figure 5. Effect of opto-electronic stimulation and sensing module implantation or sham surgery on bladder cystometric properties, histology and animal health.

a) Representative traces of anesthetized constant infusion (0.1 ml/min) cystometric voiding from sham and CLOC device implanted animals. **b)** Quantification of peak pressure (PP), base pressure (BP), and threshold pressure (TP) indicated no significant differences between sham and device groups. The data indicates no significant differences in intercontraction interval (ICI) or bladder compliance (Δvolume/Δpressure) between sham and device animals (n=6 for all groups; all data represented ± SEM) **c)** Representative H&E staining of bladder tissue in direct contact with the strain gauge and the full CLOC device implanted and sham-surgery animals (No overt histological differences were observed in these tissues (n=3 for each group in biologically independent samples with similar results). Scale bar is 100 μm. Examples (scale bar 250 μm) **(d)** and quantification **(e)** of bladder thickness, comparing device implanted animals to sham. **f)** Sham-surgery and device implanted animals gained similar amounts of weight on postoperative day (POD) 7. **g)** Animals from both groups ran similar distances in a novel arena (42 × 42 × 30 cm). **h)** CLOC system implantation did not

significantly affect measurements of gait, including average run speed, run speed variation, step sequence regularity and steps per second (cadence) (n = 5 for all groups (panel d-f); all data represented ± SEM).

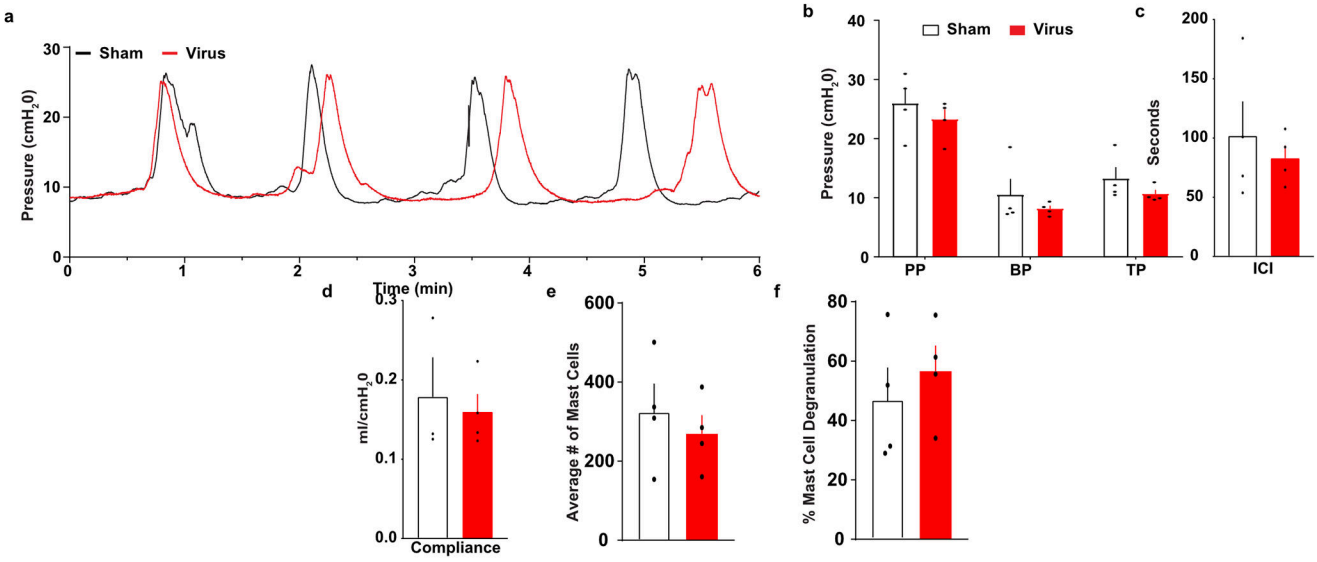

Extended Data Figure 6. Bladder cystometric properties and markers of inflammation are not significantly altered by injection of HSV-eYFP compared to sham surgery animals.

a) Representative traces of constant infusion (0.1 ml/min) anesthetized (urethane) cystometric voiding from sham-injected and virus-injected (HSV-CMV-eYFP) rats. **b)** Quantification of peak pressure (PP), base pressure (BP), and threshold pressure (TP) indicated no significant differences between sham-injected and virus-injected groups (n=4 animals per group; all data represented ± SEM). There were no significant differences in intercontraction interval (ICI) **(c)** or bladder compliance (Δvolume/Δpressure) **(d)** between sham-injected and virus-injected rats. No significant difference was observed in average number of mast cells **(e)** or degree of degranulation **(f)**, indicating that no overt inflammatory response is detected in bladders injected with HSV-eYFP vs sham surgery 7 days after injection (n=4 animals per group; all data represented ± SEM)

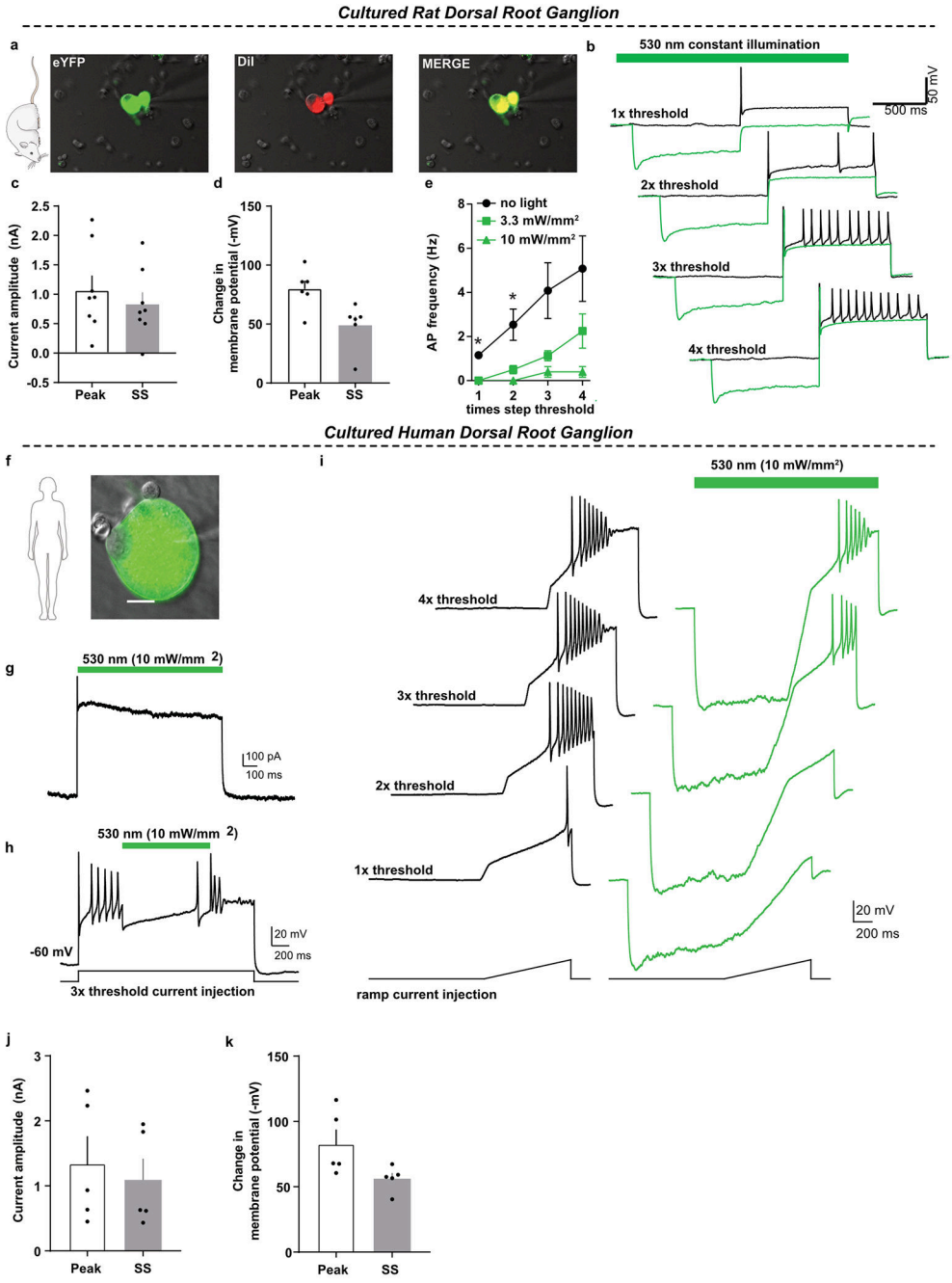

Extended Data Figure 7. Activation of Arch, in cultured bladder-projecting rat DRG neurons and human DRG reduces neuronal excitability.

a) Example of a neuron transduced with HSV-Arch-eYFP (green) and identified as a neuron that projects to bladder based on labeling with DiI (red) following DiI injection in the bladder wall (7 days prior) (scale bar 20 μM; similar to results obtained from three independent experiments). **b)** Representative traces of DRG neuron firing properties in response to step current injection current 1-4x threshold with (green) and without (black) green light illumination (530 nm) (similar to results obtained from three independent

cultures). Quantification of Arch-induced current amplitude in voltage clamp **(c)** and membrane hyperpolarization in current clamp **(d)** at peak and steady state. **e)** Quantification of action potential (AP) frequency with and without illumination demonstrating a light dependent inhibition of AP firing. (**a-e**: no light n=13, 3.3 mW/mm^2 n= 8, 10 mw/mm^2 n=5 different cells, from 3 biologically independent cultures; all data represented mean ± SEM; One-way Anova with Dunnett's multiple comparisons test; * $p<0.05$). f) Example of a patched human DRG neuron transduced with HSV-Arch-eYFP. **g)** Example voltage clamp trace demonstrating the photocurrent elicited by green light (530 nm). **h)** Representative current clamp trace demonstrating the ability of Arch to inhibit neuronal firing in response to 3× threshold current injection. **i)** Current clamp traces with (green) and without (black) activation of Arch, showing a reduction in action potential firing in response to 1-4x threshold ramp currents. Quantification of light-induced current in voltage clamp **(j)** and hyperpolarization in current clamp **(k)** at peak and steady state (SS) in Arch-expressing human DRG neurons. Panels f-h have been repeated in 5 different cells from one culture, with similar biological results. The cartoon images from panels **(a)** and **(f)** are from Servier Medical Art by Servier (https://smart.servier.com/), and are covered by Creative Commons 3.0 attribution license (https://creativecommons.org/licenses/by/3.0/). No changes were made to the original artwork.

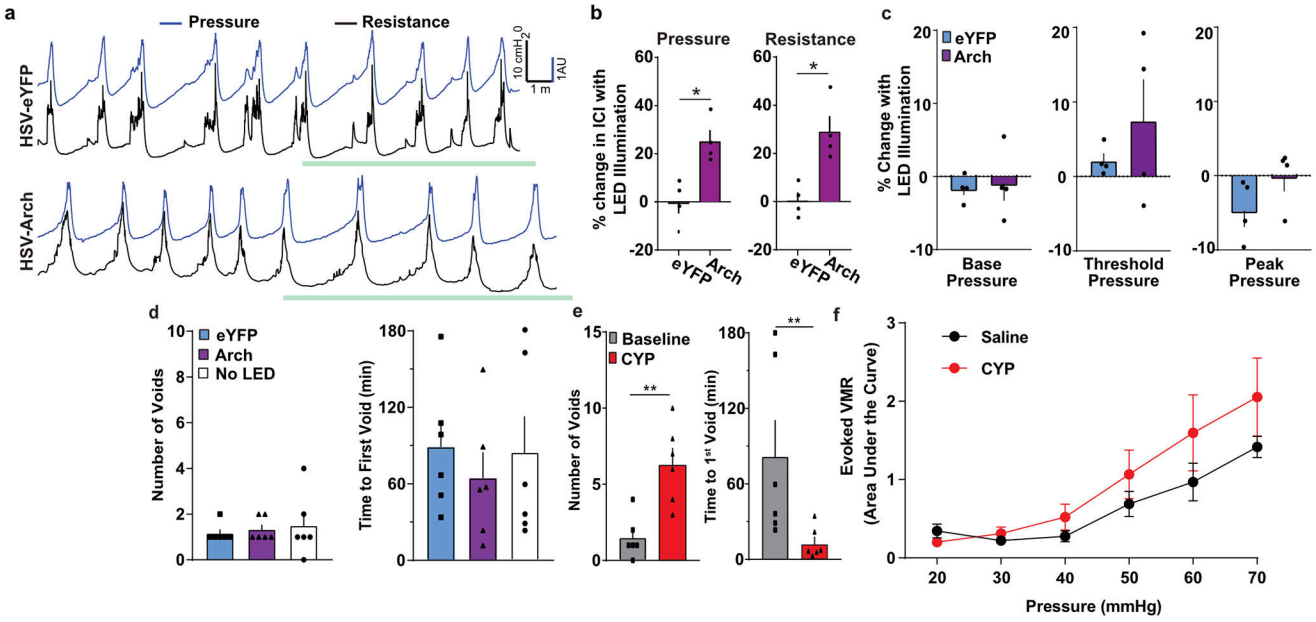

Extended Data Figure 8. Effect of Arch activation and CYP-induced bladder dysfunction on voiding properties.

Representative traces **(a)** and grouped data **(b)** that demonstrate a significant increase in cystometric inter-contraction interval (ICI) during green light illumination in HSV-Arch injected animals compared to HSV-eYFP injected controls, as defined by the strain gauge and pressure recordings. (n=4 rats/group; *$p<0.05$, unpaired t test). **c)** Activation of Arch in bladder sensory afferents does not affect base, threshold or peak pressure. No changes were observed during bladder illumination in base pressure, threshold pressure or peak pressure in

anesthetized (urethane) cystometry (0.1 ml/min) comparing HSV-Arch-eYFP injected rats to HSV-eYFP injected rats. (n=4; all data represented mean ± SEM). **d)** Effect of Arch activation on normal voiding in awake, non-anesthetized rats. Illumination of HSV-Arch injected bladders (Arch = HSV-Arch-eYFP/LED-ON) did not significantly alter number of voids or time to first void compared to HSV-eYFP (eYFP = HSV-eYFP injected/LED-ON) and HSV-injected/ No LED groups in non-inflamed animals. (n=6; all data represent mean ± SEM). **e)** Rats injected with CYP have significantly more voids and less time to 1st void during the 3 hours after CYP injection as compared to baseline. (n=6; all data represented mean ± SEM; ** p<0.01). **f)** A single dose of CYP does not cause a significant increase in evoked visceral motor response (VMR). (n=8 saline, n=9 CYP animals; data represented mean ± SEM)

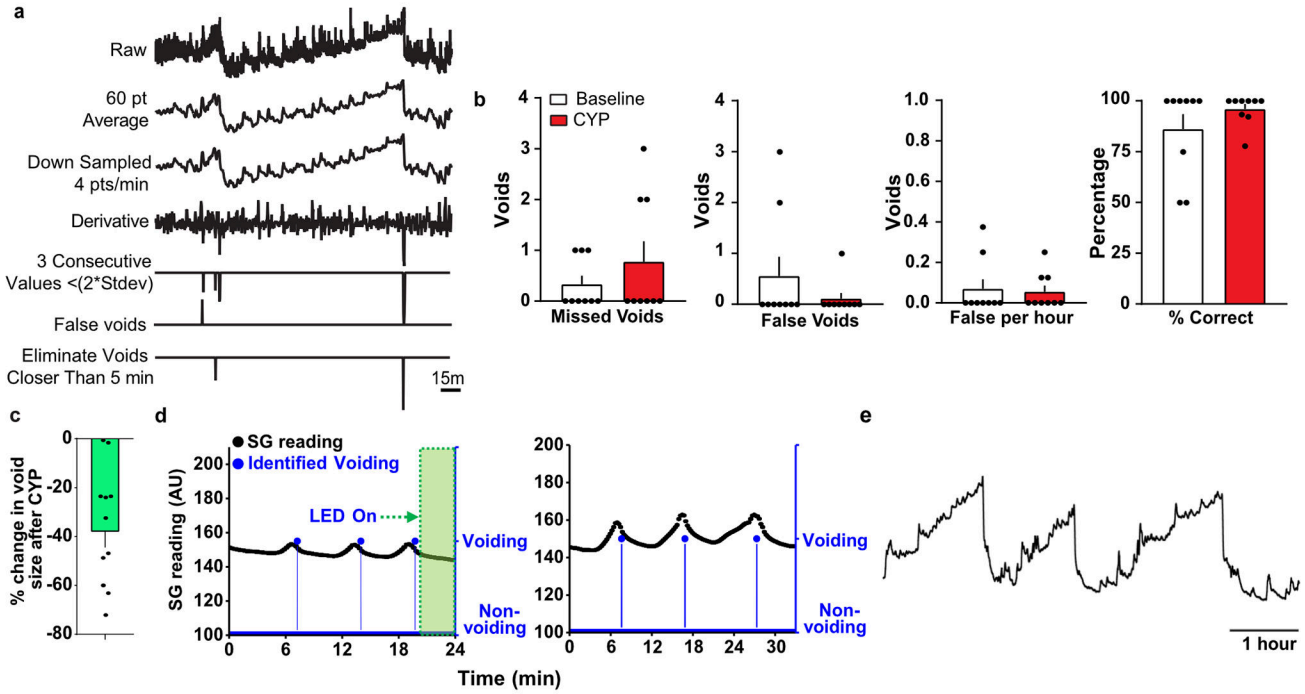

Extended Data Figure 9. Automatic identification of voiding events from raw strain gauge data. **a)** Diagram demonstrating the step-by-step process for identifying voids from raw strain gauge data. **b)** Quantification of the number of missed voids, false voids, false voids per hour and percent correct during 8 hours of recording at baseline and 8 hours after CYP using the void detection algorithm. (n=9 rat per group; data represented mean ± SEM). **c)** Percent change in void size after CYP (75 mg/kg) administration (n=11 biologically independent animals; mean ± SEM). **d)** *In-vitro* demonstration of the void volume threshold component of the closed loop algorithm. With a threshold of 15 au (20% fractional change of resistance), the closed loop system did not activate when the void volumes were larger than 15 au (right), while the closed loop system was triggered and turned on the LEDs when void sizes were smaller than 15 au (left). **e)** Demonstration of prolonged battery-free recording (repeated twice in independent animals with similar results)

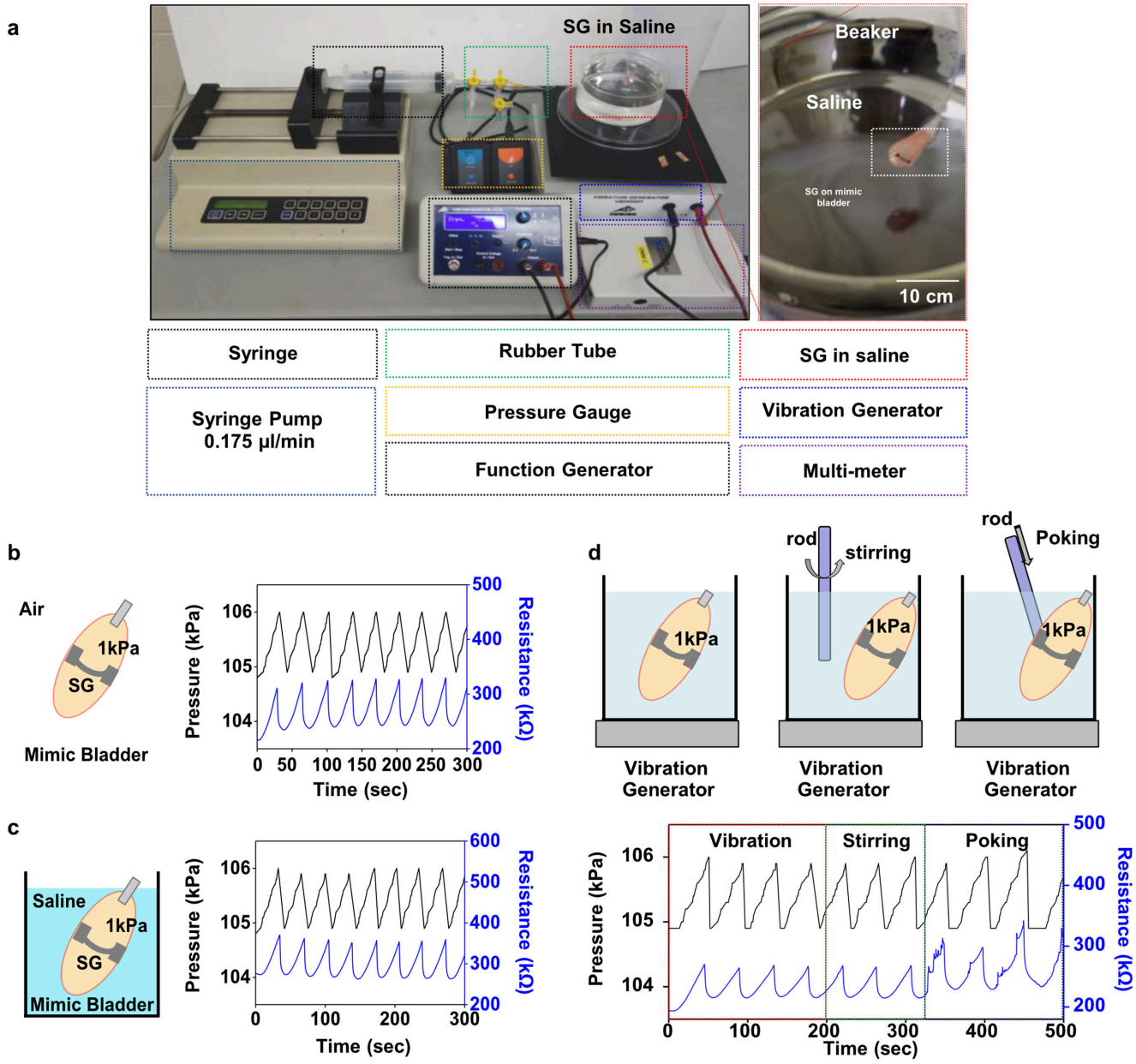

Extended Data Figure 10. Results from in vitro testing of the strain gauge.

a) Photograph of the *in vitro* setup, including a strain gauge on a mimic bladder (Ecoflex-0030) in saline solution (PH 7.4), a syringe pump (0.175 µl/min) to control the size of the bladder, a function generator to supply power (7 Hz, 10 V) for external vibration, a pressure gauge and digital multimeter to monitor pressure in the bladder. **b)** Change in resistance of strain gauge on a mimic bladder during inflation at an inner pressure of 1 kPa, in otherwise ambient laboratory condition. **c)** Similar changes during inflation with saline solution at 1 kPa, in the presence of externally induced vibration. **d)** Change in resistance change of the strain gauge under the various condition; vibration, stirring, and poking.

Supplementary Material

Refer to Web version on PubMed Central for supplementary material.

Acknowledgments:

The authors would like to acknowledge the generosity of the donor families, as well as Mid-America Transplant for making the studies of human sensory neurons possible. John Lemen provided instrumental help during human DRG surgical extractions. Additionally, we would like to thank Janet Sinn-Hanlon, The DesignGroup@VetMed, University of Illinois at Urbana-Champaign for the illustrations, Lori Strong for her technical assistance with the CT imaging, Sherri Vogt for invaluable technical support and Clint Morgan for his early input on the project.

Funding: This work was funded by an NIH Director's Transformative Research Award TR01 NS081707 (RWG and JAR), NIH SPARC Award via the NIBIB of the NIH award U18 EB021793 (RWG and JAR), R01 NS42595 (RWG), NRSA F32 DK115122 (ADM), the McDonnell Center for Cellular and Molecular Neurobiology Postdoctoral Fellowship (ADM), K01 DK115634 (VKS), the Urology Care Foundation Research Scholars Program and Kailash Kedia Research Scholar Endowment (VKS), NSF Grant-1635443 (YH), the Ryan Fellowship and the Northwestern University International Institute for Nanotechnology (YX), T32 DA007261 (LAM), T32 DK108742 (KWM), DK082315 (HHL) and K08 DK094964 to (HHL).

Refrences:

1. Birmingham K et al. Bioelectronic medicines: a research roadmap. Nature reviews. Drug discovery 13, 399–400, doi:10.1038/nrd4351 (2014). [PubMed: 24875080]
2. Cameron T Safety and efficacy of spinal cord stimulation for the treatment of chronic pain: a 20-year literature review. Journal of neurosurgery 100, 254–267 (2004). [PubMed: 15029914]
3. De Ferrari GM et al. Chronic vagus nerve stimulation: a new and promising therapeutic approach for chronic heart failure. European heart journal 32, 847–855, doi:10.1093/eurheartj/ehq391 (2011). [PubMed: 21030409]
4. de Groat WC & Tai C Impact of Bioelectronic Medicine on the Neural Regulation of Pelvic Visceral Function. Bioelectronic medicine 2015, 25–36 (2015). [PubMed: 26491706]
5. Famm K, Litt B, Tracey KJ, Boyden ES & Slaoui M Drug discovery: a jump-start for electroceuticals. Nature 496, 159–161, doi:10.1038/496159a (2013). [PubMed: 23579662]
6. Janknegt RA et al. Long-term effectiveness of sacral nerve stimulation for refractory urge incontinence. European urology 39, 101–106, doi:10.1159/000052420 (2001). [PubMed: 11173947]
7. Siegel SW et al. Long-term results of a multicenter study on sacral nerve stimulation for treatment of urinary urge incontinence, urgency-frequency, and retention. Urology 56, 87–91 (2000).
8. Kavvadias T, Huebner M, Brucker SY & Reisenauer C Management of device-related complications after sacral neuromodulation for lower urinary tract disorders in women: a single center experience. Archives of gynecology and obstetrics 295, 951–957, doi:10.1007/s00404-017-4303-2 (2017). [PubMed: 28255769]
9. del Valle J & Navarro X Interfaces with the peripheral nerve for the control of neuroprostheses. International review of neurobiology 109, 63–83, doi:10.1016/B978-0-12-420045-6.00002-X (2013). [PubMed: 24093606]
10. Rossini PM et al. Double nerve intraneural interface implant on a human amputee for robotic hand control. Clinical neurophysiology : official journal of the International Federation of Clinical Neurophysiology 121, 777–783, doi:10.1016/j.clinph.2010.01.001 (2010). [PubMed: 20110193]
11. Yoshida K, Farina D, Akay M & Jensen W Multichannel Intraneural and Intramuscular Techniques for Multiunit Recording and Use in Active Prostheses. Proceedings of the IEEE 98, 432–449, doi: 10.1109/JPROC.2009.2038613 (2010).
12. Miftahof R & Nam HG Biomechanics of the human urinary bladder. (Springer, 2013).
13. Mattis J et al. Principles for applying optogenetic tools derived from direct comparative analysis of microbial opsins. Nature methods 9, 159–172, doi:10.1038/nmeth.1808 (2011). [PubMed: 22179551]

14. Zerboni L et al. Herpes simplex virus 1 tropism for human sensory ganglion neurons in the severe combined immunodeficiency mouse model of neuropathogenesis. Journal of virology 87, 2791–2802, doi:10.1128/JVI.01375-12 (2013). [PubMed: 23269807]
15. Beaudry H, Daou I, Ase AR, Ribeiro-da-Silva A & Seguela P Distinct behavioral responses evoked by selective optogenetic stimulation of the major TRPV1+ and MrgD+ subsets of C-fibers. Pain 158, 2329–2339, doi:10.1097/j.pain.0000000000001016 (2017). [PubMed: 28708765]
16. Boada MD et al. Fast-conducting mechanoreceptors contribute to withdrawal behavior in normal and nerve injured rats. Pain 155, 2646–2655, doi:10.1016/j.pain.2014.09.030 (2014). [PubMed: 25267211]
17. Iyer SM et al. Virally mediated optogenetic excitation and inhibition of pain in freely moving nontransgenic mice. Nature biotechnology 32, 274–278, doi:10.1038/nbt.2834 (2014).
18. Iyer SM et al. Optogenetic and chemogenetic strategies for sustained inhibition of pain. Scientific reports 6, 30570, doi:10.1038/srep30570 (2016). [PubMed: 27484850]
19. Li B et al. A novel analgesic approach to optogenetically and specifically inhibit pain transmission using TRPV1 promoter. Brain research 1609, 12–20, doi:10.1016/j.brainres.2015.03.008 (2015). [PubMed: 25797803]
20. Montgomery KL et al. Wirelessly powered, fully internal optogenetics for brain, spinal and peripheral circuits in mice. Nature methods 12, 969–974, doi:10.1038/nmeth.3536 (2015). [PubMed: 26280330]
21. Towne C, Montgomery KL, Iyer SM, Deisseroth K & Delp SL Optogenetic control of targeted peripheral axons in freely moving animals. PloS one 8, e72691, doi:10.1371/journal.pone.0072691 (2013). [PubMed: 23991144]
22. DeBerry JJ et al. Differential Regulation of Bladder Pain and Voiding Function by Sensory Afferent Populations Revealed by Selective Optogenetic Activation. Front Integr Neurosci 12, 5, doi:10.3389/fnint.2018.00005 (2018). [PubMed: 29483864]
23. ClinicalTrials.Gov. RST-001 Phase I/II Trial for Advanced Retinitis Pigmentosa. https://ClinicalTrials.gov/show/NCT02556736 (2018).
24. ClinicalTrials.Gov. Dose-escalation Study to Evaluate the Safety and Tolerability of GS030 in Subjects With Retinitis Pigmentosa. https://ClinicalTrials.gov/show/NCT03326336 (2018).
25. Chuong AS et al. Noninvasive optical inhibition with a red-shifted microbial rhodopsin. Nature neuroscience 17, 1123–1129, doi:10.1038/nn.3752 (2014). [PubMed: 24997763]
26. Lin JY, Knutsen PM, Muller A, Kleinfeld D & Tsien RY ReaChR: a red-shifted variant of channelrhodopsin enables deep transcranial optogenetic excitation. Nature neuroscience 16, 1499–1508, doi:10.1038/nn.3502 (2013). [PubMed: 23995068]

Method References:

27. Christian AG & Ellis M Low-cost carbon thick-film strain sensors for implantable applications. Journal of Micromechanics and Microengineering 20, 095028 (2010).
28. Lu N, Lu C, Yang S & Rogers J Highly Sensitive Skin-Mountable Strain Gauges Based Entirely on Elastomers. Advanced Functional Materials 22, 4044–4050, doi:doi:10.1002/adfm.201200498 (2012).
29. Damaser MS & Lehman SL Does it matter, the shape of the bladder? Neurourology and urodynamics 12, 277–280 (1993). [PubMed: 8330051]
30. Korkmaz I & Rogg B A simple fluid-mechanical model for the prediction of the stress-strain relation of the male urinary bladder. Journal of biomechanics 40, 663–668, doi:10.1016/j.jbiomech.2006.02.014 (2007). [PubMed: 16631761]
31. Kelly P Mechanics Lecture Notes: An introduction to Solid Mechanics. Available from http://homepages.engineering.auckland.ac.nz/~pkel015/SolidMechanicsBooks/index.html, p 185–194 (2018).
32. Ren Y, Qi H, Chen Q & Ruan L Thermal dosage investigation for optimal temperature distribution in gold nanoparticle enhanced photothermal therapy. International Journal of Heat and Mass Transfer 106, 212–221, doi:10.1016/j.ijheatmasstransfer.2016.10.067 (2017).

33. Samineni VK et al. Fully implantable, battery-free wireless optoelectronic devices for spinal optogenetics. Pain 158, 2108–2116, doi:10.1097/j.pain.0000000000000968 (2017). [PubMed: 28700536]
34. Bhattacharya A & Mahajan RL in BiOS 2001 The International Symposium on Biomedical Optics. 10 (SPIE).
35. Liu J, Zhu L & Xu LX Studies on the three-dimensional temperature transients in the canine prostate during transurethral microwave thermal therapy. Journal of biomechanical engineering 122, 372–379 (2000). [PubMed: 11036560]
36. Uvin P et al. The use of cystometry in small rodents: a study of bladder chemosensation. Journal of visualized experiments : JoVE, e3869, doi:10.3791/3869 (2012). [PubMed: 22929055]
37. Andersson KE, Soler R & Fullhase C Rodent models for urodynamic investigation. Neurourology and urodynamics 30, 636–646, doi:10.1002/nau.21108 (2011). [PubMed: 21661007]
38. Samineni VK et al. Optogenetic silencing of nociceptive primary afferents reduces evoked and ongoing bladder pain. Scientific reports 7, 15865, doi:10.1038/s41598-017-16129-3 (2017). [PubMed: 29158567]
39. Park SI et al. Soft, stretchable, fully implantable miniaturized optoelectronic systems for wireless optogenetics. Nature biotechnology 33, 1280–1286, doi:10.1038/nbt.3415 (2015).
40. Valtcheva MV et al. Surgical extraction of human dorsal root ganglia from organ donors and preparation of primary sensory neuron cultures. Nature protocols 11, 1877–1888, doi:10.1038/nprot.2016.111 (2016). [PubMed: 27606776]
41. Lai H et al. Animal Models of Urologic Chronic Pelvic Pain Syndromes: Findings From the Multidisciplinary Approach to the Study of Chronic Pelvic Pain Research Network. Urology 85, 1454–1465, doi:10.1016/j.urology.2015.03.007 (2015). [PubMed: 26099889]
42. Parsons BA & Drake MJ Animal models in overactive bladder research. Handb Exp Pharmacol, 15–43, doi:10.1007/978-3-642-16499-6_2 (2011). [PubMed: 21290220]
43. Crock LW et al. Central amygdala metabotropic glutamate receptor 5 in the modulation of visceral pain. J Neurosci 32, 14217–14226, doi:10.1523/JNEUROSCI.1473-12.2012 (2012). [PubMed: 23055491]

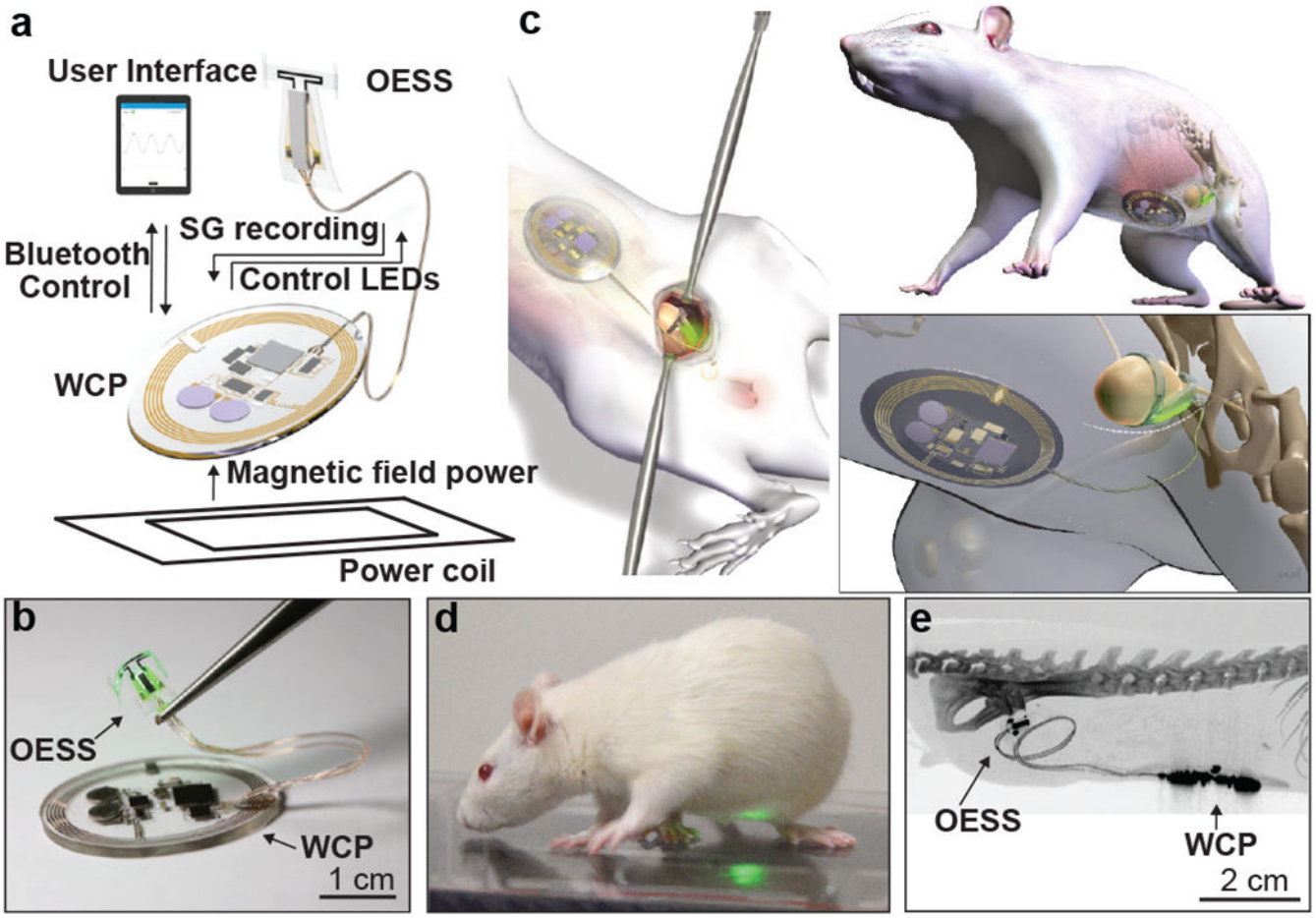

Figure 1. Schematic illustrations and images of a fully implantable, soft optoelectronic system for wireless, closed-loop optogenetic modulation of bladder function.

a) The platform consists an opto-electronic stimulation and sensing (OESS) module, a low modulus, stretchable strain gauge (SG) with integrated microscale inorganic light emitting diodes (μ-ILEDs) that wraps around the bladder to monitor changes in its volume and to provide optogenetic stimulation to the neurons innervating the bladder. The wireless control/power (WCP) module records the response of the strain gauge, controls operation of the μ-ILEDs and provides power management. Wireless data communication to and from the WCP module relies on Bluetooth protocols and a tablet computer. Power is delivered wirelessly via resonant magnetic coupling through a dual antenna transmitter. **b)** Picture of opto-electronic stimulation and sensing module including the strain gauge, the μ-ILEDs and wireless base station for data communication. **c)** Schematic illustration that highlights the placement of the strain gauge around the bladder, with an implanted, wired connection to the WCP module subcutaneously implanted anterior to the bladder. Images created by Janet Sinn-Hanlon, The DesignGroup@VetMed, University of Illinois at Urbana-Champaign. **d)** Rat implanted with the complete system (a green μ-ILED indicator on the WCP module verifies function). **e)** Computed tomography image of a device implanted for 1 month.

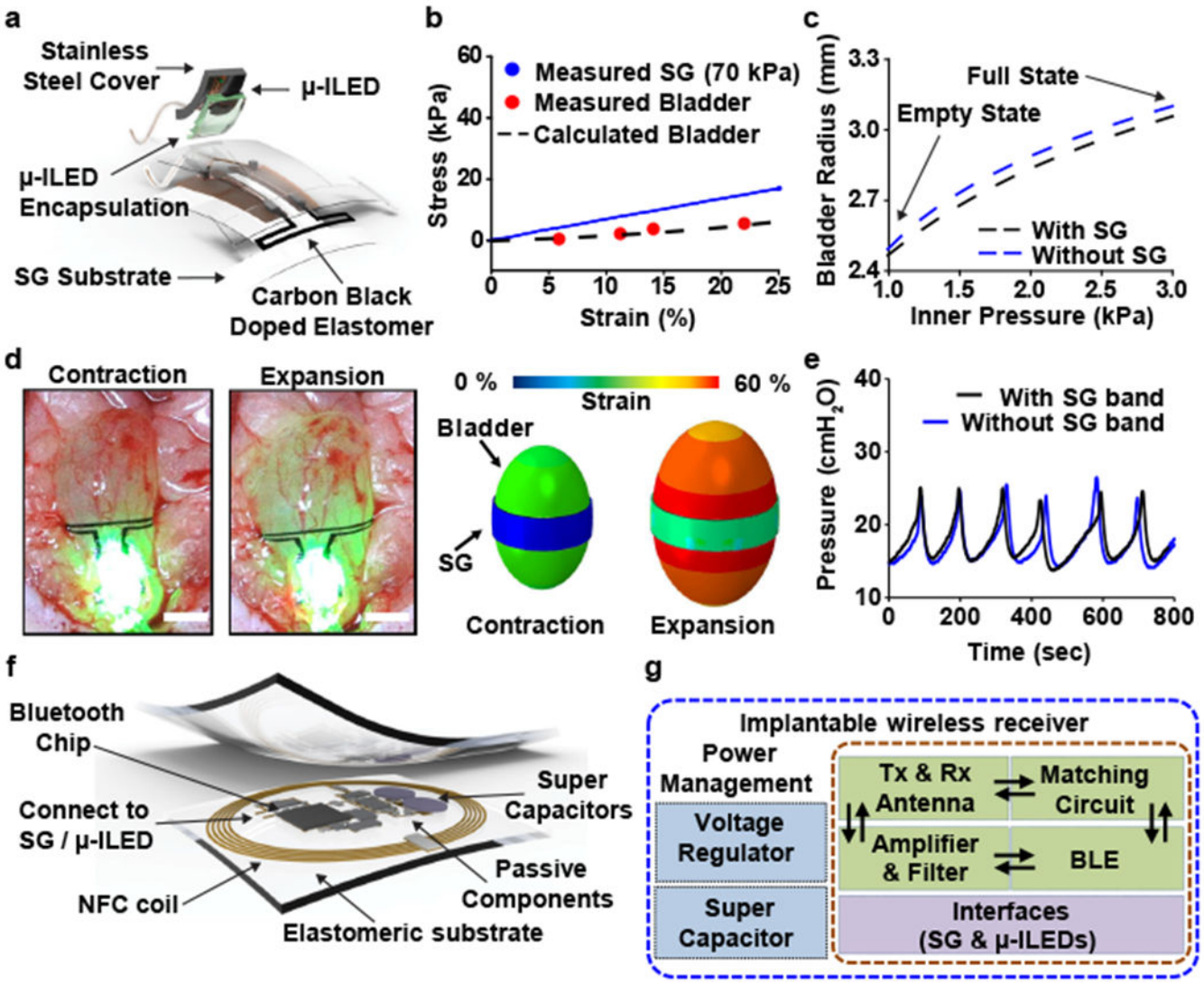

Figure 2. Electrical and mechanical properties of the opto-electronic stimulation and sensing module.

a) Schematic illustration of the opto-electronic stimulation and sensing module. **b)** Dynamic mechanical analysis of a strain gauge (SG) with comparison to a simulated stress-strain curve of bladder from the empty state. **c)** Simulated radius of a bladder during expansion with and without an integrated opto-electronic stimulation and sensing module. **d)** Images (left) of a strain gauge and a pair of μ-ILEDs wrapped around the outer surface of the rat bladder, in contracted and expanded states. Computed distributions of strain (right) for a strain gauge integrated with a spheroidal model of the rat bladder. (Scale bar: 2.5mm) **e)** Acute rat bladder cystometry before and after placement of the opto-electronic stimulation and sensing module, demonstrating no discernable alterations to intravesical pressure. **f)** Schematic illustration of the implantable wireless control/power module. **g)** Operational block diagram of the overall system design. (Rx-receiving, Tx-transmitting)

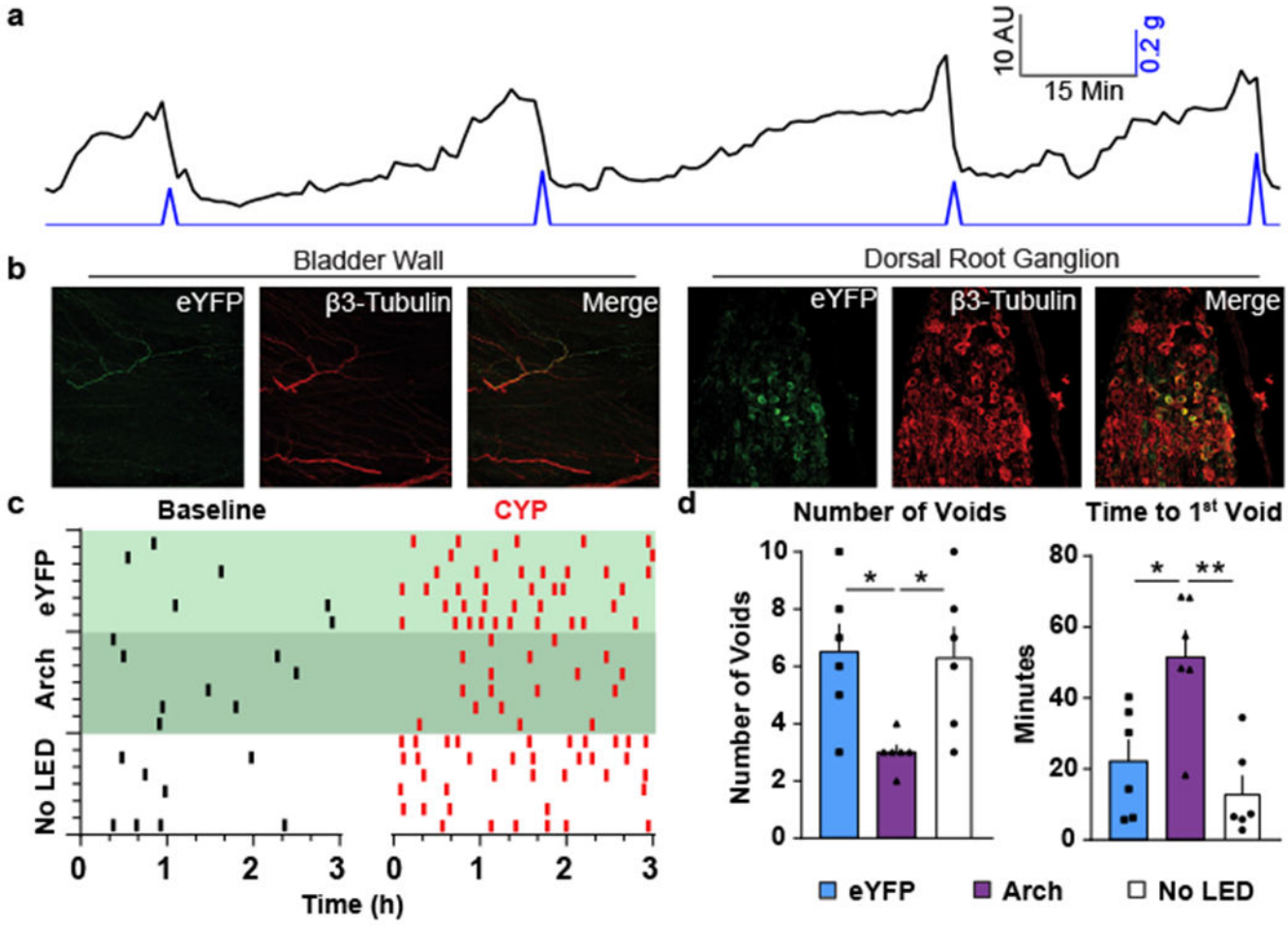

Figure 3. Optogenetic modulation of bladder function.

a) Time dependence of strain gauge data (60 point running average) collected from a freely moving rat implanted with a CLOC system, showing rapid decreases in resistance that correlate with micturition events measured by a computerized balance in a micturition cage. **b)** Expression of Arch-eYFP in bladder afferent endings and cell bodies of the dorsal root ganglion 7 days after injection of HSV-Arch-eYFP into the bladder wall. **c)** Raster plot representing voiding of individual animals (horizontal rows) before and after CYP in HSV-eYFP LED-ON, HSV-Arch LED-ON and virus-injected LED-OFF groups before and after CYP. **d)** Quantification of mean number of voids 3 hours after CYP and time to 1st void after CYP injection in all groups. (n=6 rats/group; *p<0.05, **p<0.01; Two-way ANOVA with Tukey's multiple comparison test; Error bars represent Mean±SEM).

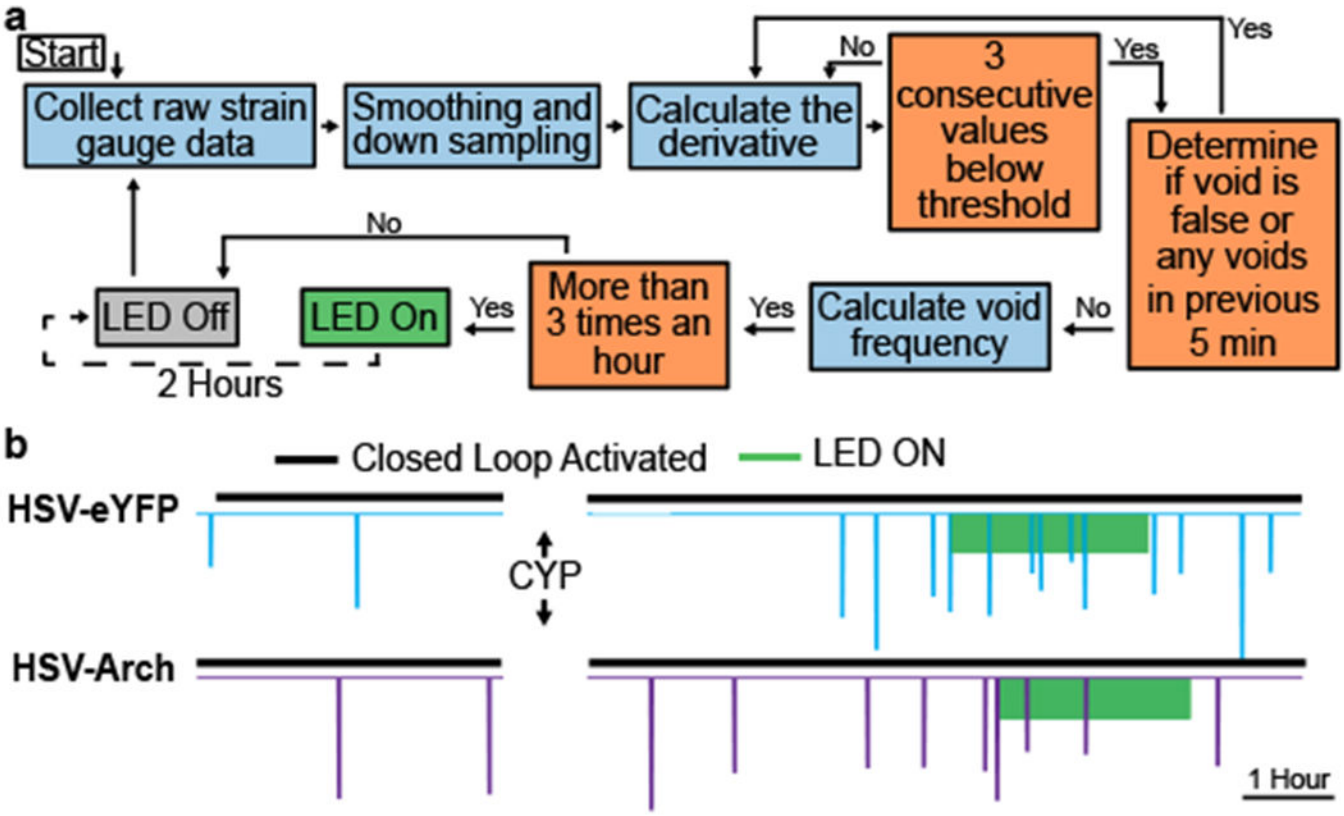

Figure 4. Closed-loop optogenetic control of bladder function.

a) Flow chart of the steps implemented in the closed-loop software to activate the μ-ILED when voiding becomes hyperactive. **b)** Demonstration of closed-loop μ-ILED activation, initiated at an average of 265 min post-injection after injection of CYP with corresponding decrease in voiding events in HSV-Arch-eYFP injected rats compared to HSV-eYFP control injected rats.